Draft version August 9, 2016
Preprint typeset using LaTeX style emulateapj v. 5/2/11

THE THIRTEENTH DATA RELEASE OF THE SLOAN DIGITAL SKY SURVEY: FIRST SPECTROSCOPIC DATA FROM THE SDSS-IV SURVEY MAPPING NEARBY GALAXIES AT APACHE POINT OBSERVATORY

Franco D. Albareti[1,2,3], Carlos Allende Prieto[4,5], Andres Almeida[6], Friedrich Anders[7], Scott Anderson[8],
Brett H. Andrews[9], Alfonso Aragón-Salamanca[10], Maria Argudo-Fernández[11,12], Eric Armengaud[13],
Eric Aubourg[14], Vladimir Avila-Reese[15], Carles Badenes[9], Stephen Bailey[16], Beatriz Barbuy[17,18],
Kat Barger[19], Jorge Barrera-Ballesteros[20], Curtis Bartosz[8], Sarbani Basu[21], Dominic Bates[22],
Giuseppina Battaglia[4,5], Falk Baumgarten[7,23], Julien Baur[13], Julian Bautista[24], Timothy C. Beers[25],
Francesco Belfiore[26,27], Matthew Bershady[28], Sara Bertran de Lis[4,5], Jonathan C. Bird[29],
Dmitry Bizyaev[30,31,32], Guillermo A. Blanc[33,34,35], Michael Blanton[36], Michael Blomqvist[37], Adam S. Bolton[38,24],
J. Borissova[39,40], Jo Bovy[41,42], William Nielsen Brandt[43,44,45], Jonathan Brinkmann[30], Joel R. Brownstein[24],
Kevin Bundy[46], Etienne Burtin[13], Nicolás G. Busca[14], Hugo Orlando Camacho Chavez[47,18], M. Cano Díaz[15],
Michele Cappellari[48], Ricardo Carrera[4,5], Yanping Chen[49], Brian Cherinka[20], Edmond Cheung[46],
Cristina Chiappini[7], Drew Chojnowski[31], Chia-Hsun Chuang[7], Haeun Chung[50], Rafael Fernando Cirolini[51,18],
Nicolas Clerc[52], Roger E. Cohen[53], Julia M. Comerford[54], Johan Comparat[1,2], Marie-Claude Cousinou[55],
Kevin Covey[56], Jeffrey D. Crane[33], Rupert Croft[57], Katia Cunha[58], Luiz da Costa[18,58],
Gabriele da Silva Ilha[51,18], Jeremy Darling[54], James W. Davidson Jr.[59], Kyle Dawson[24], Nathan De Lee[60,29],
Axel de la Macorra[15], Sylvain de la Torre[37], Alice Deconto Machado[51,18], Timothée Delubac[61],
Aleksandar M. Diamond-Stanic[28], John Donor[19], Juan Jose Downes[15,62], Niv Drory[63],
Hélion du Mas des Bourboux[13], Cheng Du[64], Tom Dwelly[52], Garrett Ebelke[59], Arthur Eigenbrot[28],
Daniel J. Eisenstein[65], Yvonne P. Elsworth[66,67], Eric Emsellem[68,69], Michael Eracleous[43,44],
Stephanie Escoffier[55], Michael L. Evans[8], Jesús Falcón-Barroso[4,5], Xiaohui Fan[70], Ginevra Favole[1,2],
Emma Fernández-Alvar[15], J. G. Fernández-Trincado[71], Diane Feuillet[31], Scott W. Fleming[72,73],
Andreu Font-Ribera[16,46], Gordon Freischlad[30,31], Peter Frinchaboy[19], Hai Fu[74], Yang Gao (高扬)[12],
D. A. García-Hernández[4,5], Ana E. García Pérez[4,5], Rafael A. García[75], R. Garcia-Dias[4,5], Patrick Gaulme[30,31],
Junqiang Ge[76], Douglas Geisler[53], Hector Gil Marin[77,78], Bruce Gillespie[20], Léo Girardi[79,18],
Daniel Goddard[80], Yilen Gómez Maqueo Chew[15], Violeta Gonzalez-Perez[80], Kathleen Grabowski[30,31],
Paul Green[65], Thomas Grier[19,81], Catherine J. Grier[43,44], Hong Guo[12], Julien Guy[82], Alex Hagen[43,44],
Matt Hall[59], Paul Harding[83], R. E. Harley[56], Sten Hasselquist[31], Suzanne Hawley[8], Christian R. Hayes[59],
Fred Hearty[43], Saskia Hekker[84], Hector Hernandez Toledo[15], Shirley Ho [57,16], David W. Hogg[36],
Kelly Holley-Bockelmann[29], Jon A. Holtzman[31], Parker H. Holzer[24], Jian Hu (胡剑)[64], Daniel Huber[85,86,67],
Timothy Alan Hutchinson[24], Ho Seong Hwang[50], Héctor J. Ibarra-Medel[15], Inese I. Ivans[24], KeShawn Ivory[19,87],
Kurt Jaehnig[28], Trey W. Jensen[24], Jennifer A. Johnson[88,89], Amy Jones[90], Eric Jullo[37], T. Kallinger[91],
Karen Kinemuchi[30,31], David Kirkby[92], Mark Klaene[30], Jean-Paul Kneib[61], Juna A. Kollmeier[33], Ivan Lacerna[93],
Richard R. Lane[93], Dustin Lang[42], Pierre Laurent[13], David R. Law[72], Jean-Marc Le Goff[13],
Alexie Leauthaud[46], Cheng Li[12,64], Ran Li[76], Chen Li[12], Niu Li[64], Fu-Heng Liang (梁赋珩)[64], Yu Liang[64],
Marcos Lima[47,18], Lihwai Lin (林俐暉)[94], Lin Lin (林琳)[12], Yen-Ting Lin (林彥廷)[94], Dan Long[30],
Sara Lucatello[79], Nicholas MacDonald[8], Chelsea L. MacLeod[65], J. Ted Mackereth[95], Suvrath Mahadevan[43],
Marcio Antonio-Geimba Maia[18,58], Roberto Maiolino[26,27], Steven R. Majewski[59], Olena Malanushenko[30,31],
Nícolas Dullius Mallmann[96,18], Arturo Manchado[4,5,97], Claudia Maraston[80], Rui Marques-Chaves[4,5],
Inma Martinez Valpuesta[4,5], Karen L. Masters[80], Savita Mathur[98], Ian D. McGreer[70], Andrea Merloni[52],
Michael R. Merrifield[10], Szabolcs Mészáros[99], Andres Meza[100], Andrea Miglio[66], Ivan Minchev[7],
Karan Molaverdikhani[54,101], Antonio D. Montero-Dorta[24], Benoit Mosser[102], Demitri Muna[88,89], Adam Myers[103],
Preethi Nair[104], Kirpal Nandra[52], Melissa Ness[101], Jeffrey A. Newman[9], Robert C. Nichol[80],
David L. Nidever[70], Christian Nitschelm[11], Julia O'Connell[19], Audrey Oravetz[30,31], Nelson Padilla[93],
Nathalie Palanque-Delabrouille[13], Kaike Pan[30,31], John Parejko[8], Isabelle Pâris[37], John A. Peacock[105],
Sebastien Peirani[106,46], Marcos Pellejero-Ibanez[4,5], Samantha Penny[80], Will J. Percival[80],
Jeffrey W. Percival[28], Ismael Perez-Fournon[4,5], Patrick Petitjean[106], Matthew Pieri[37],
Marc H. Pinsonneault[88], Alice Pisani[55,106], Francisco Prada[1,2,107], Abhishek Prakash[9], Natalie Price-Jones[42],
M. Jordan Raddick[20], Mubdi Rahman[20], Anand Raichoor[13], Sandro Barboza Rembold[51,18], A. M. Reyna[56],
James Rich[13], Hannah Richstein[19], Jethro Ridl[52], Rogério Riffel[96,18], Rogemar A. Riffel[51,18],
Hans-Walter Rix[101], Annie C. Robin[71], Constance M. Rockosi[108], Sergio Rodríguez-Torres[1],
Thaíse S. Rodrigues[79,109,18], Natalie Roe[16], A. Roman Lopes[6], Carlos Román-Zúñiga[110], Ashley J. Ross[89],
Graziano Rossi[111], John Ruan[8], Rossana Ruggeri[80], Jessie C. Runnoe[43,44], Salvador Salazar-Albornoz[52],
Mara Salvato[52], Ariel G. Sánchez[52], Sebastian F. Sanchez[15], José R. Sánchez-Gallego[8],
Basílio Xavier Santiago[96,18], Ricardo Schiavon[95], Jaderson S. Schimoia[96,18], Eddie Schlafly[16,112],
David J. Schlegel[16], Donald P. Schneider[43,44], Ralph Schoenrich[48], Mathias Schultheis[113], Axel Schwope[7],
Hee-Jong Seo[114], Aldo Serenelli[115], Branimir Sesar[101], Zhengyi Shao[12], Matthew Shetrone[116], Michael Shull[54],
Victor Silva Aguirre[67], M. F. Skrutskie[59], Anže Slosar[117], Michael Smith[28], Verne V. Smith[118],
Jennifer Sobeck[59], Garrett Somers[88,29], Diogo Souto[58], David V. Stark[46], Keivan G. Stassun[29],
Matthias Steinmetz[7], Dennis Stello[85,119], Thaisa Storchi Bergmann[96,18], Michael A. Strauss[120],
Alina Streblyanska[4,5], Guy S. Stringfellow[54], Genaro Suárez[110], Jing Sun[19], Manuchehr Taghizadeh-Popp[20],
Baitian Tang[53], Charling Tao[64,55], Jamie Tayar[88], Mita Tembe[59], Daniel Thomas[80], Jeremy Tinker[36],
Rita Tojeiro[22], Christy Tremonti[28], Nicholas Troup[59], Jonathan R. Trump[43,112], Eduardo Unda-Sanzana[11],
O. Valenzuela[15], Remco van den Bosch[101], Mariana Vargas-Magaña[121], Jose Alberto Vazquez[117],

Sandro Villanova[53], M. Vivek[24], Nicole Vogt[31], David Wake[28,122], Rene Walterbos[31], Yuting Wang[76,80], Enci Wang[12], Benjamin Alan Weaver[36], Anne-Marie Weijmans[22], David H. Weinberg[88,89], Kyle B. Westfall[80], David G. Whelan[123], Eric Wilcots[28], Vivienne Wild[22], Rob A. Williams[95], John Wilson[59], W. M. Wood-Vasey[9], Dominika Wylezalek[20], Ting Xiao (肖婷)[12], Renbin Yan[124], Meng Yang[64], Jason E. Ybarra[110,125], Christophe Yèche[13], Fang-Ting Yuan[12], Nadia Zakamska[20], Olga Zamora[4,5], Gail Zasowski[20], Kai Zhang[124], Cheng Zhao[64], Gong-Bo Zhao[76,80] Zheng Zheng[24], Zheng Zheng[76], Zhi-Min Zhou[76], Guangtun Zhu[20,112], Joel C. Zinn[88], Hu Zou[76]

Draft version August 9, 2016

Abstract

The fourth generation of the Sloan Digital Sky Survey (SDSS-IV) began observations in July 2014. It pursues three core programs: the Apache Point Observatory Galactic Evolution Experiment 2 (APOGEE-2), Mapping Nearby Galaxies at APO (MaNGA), and the Extended Baryon Oscillation Spectroscopic Survey (eBOSS). As well as its core program, eBOSS contains two major subprograms: the Time Domain Spectroscopic Survey (TDSS) and the SPectroscopic IDentification of ERosita Sources (SPIDERS). This paper describes the first data release from SDSS-IV, Data Release 13 (DR13), which contains new data, reanalysis of existing data sets and, like all SDSS data releases, is inclusive of previously released data. DR13 makes publicly available 1390 spatially resolved integral field unit observations of nearby galaxies from MaNGA, the first data released from this survey. It includes new observations from eBOSS, completing the Sloan Extended QUasar, Emission-line galaxy, Luminous red galaxy Survey (SEQUELS). In addition to targeting galaxies and quasars, SEQUELS also targeted variability-selected objects from TDSS and X-ray selected objects from SPIDERS. DR13 includes new reductions of the SDSS-III BOSS data, improving the spectrophotometric calibration and redshift classification. DR13 releases new reductions of the APOGEE-1 data from SDSS-III, with abundances of elements not previously included and improved stellar parameters for dwarf stars and cooler stars. For the SDSS imaging data, DR13 provides new, more robust and precise photometric calibrations. Several value-added catalogs are being released in tandem with DR13, in particular target catalogs relevant for eBOSS, TDSS, and SPIDERS, and an updated red-clump catalog for APOGEE. This paper describes the location and format of the data now publicly available, as well as providing references to the important technical papers that describe the targeting, observing, and data reduction. The SDSS website, www.sdss.org, provides links to the data, tutorials and examples of data access, and extensive documentation of the reduction and analysis procedures. DR13 is the first of a scheduled set that will contain new data and analyses from APOGEE-2, MaNGA, eBOSS, TDSS, and SPIDERS from the planned 6-year operations of SDSS-IV.

Subject headings: Atlases — Catalogs — Surveys

[1] Instituto de Física Teórica, (UAM/CSIC), Universidad Autónoma de Madrid, Cantoblanco, E-28049 Madrid, Spain

[2] Campus of International Excellence UAM+CSIC, Cantoblanco, E-28049 Madrid, Spain

[3] la Caixa-Severo Ochoa Scholar

[4] Instituto de Astrofísica de Canarias, E-38205 La Laguna, Tenerife, Spain

[5] Departamento de Astrofísica, Universidad de La Laguna (ULL), E-38206 La Laguna, Tenerife, Spain

[6] Departamento de Fisica y Astronomia, Universidad de La Serena, Cisternas 1200, La Serena, 0000-0002-1379-4204, Chile

[7] Leibniz-Institut f´ur Astrophysik Potsdam (AIP), An der Sternwarte 16, D-14482 Potsdam, Germany

[8] Department of Astronomy, University of Washington, Box 351580, Seattle, WA 98195, USA

[9] PITT PACC, Department of Physics and Astronomy, University of Pittsburgh, Pittsburgh, PA 15260, USA

[10] School of Physics and Astronomy, University of Nottingham, University Park, Nottingham, NG7 2RD, UK

[11] Unidad de Astronomía, Universidad de Antofagasta, Avenida Angamos 601, Antofagasta 1270300, Chile

[12] Shanghai Astronomical Observatory, Chinese Academy of Science, 80 Nandan Road, Shanghai 200030, P. R. China

[13] IRFU, CEA, Centre d'Etudes Saclay, 91191 Gif-Sur-Yvette Cedex, France

[14] APC, University of Paris Diderot, CNRS/IN2P3, CEA/IRFU, Observatoire de Paris, Sorbonne Paris Cite, France

[15] Instituto de Astronomía, Universidad Nacional Autónoma de México, Apartado Postal 70-264, México D.F., 04510 Mexico

[16] Lawrence Berkeley National Laboratory, 1 Cyclotron Road, Berkeley, CA 94720, USA

[17] Universidade de São Paulo, IAG, Rua do Matão 1226, São Paulo 05508-900, Brazil

[18] Laboratório Interinstitucional de e-Astronomia - LIneA, Rua Gal. José Cristino 77, Rio de Janeiro, RJ - 20921-400, Brazil

[19] Department of Physics & Astronomy, Texas Christian University, Fort Worth, TX 76129, USA

[20] Center for Astrophysical Sciences, Department of Physics and Astronomy, Johns Hopkins University, 3400 North Charles Street, Baltimore, MD 21218, USA

[21] Department of Astronomy, Yale University, 52 Hillhouse Avenue, New Haven, CT 06511, USA

[22] School of Physics and Astronomy, University of St Andrews, North Haugh, St Andrews KY16 9SS, UK

[23] Humboldt-Universität zu Berlin, Institut für Physik, Newtonstrasse 15,D-12589, Berlin, Germany

[24] Department of Physics and Astronomy, University of Utah, 115 S. 1400 E., Salt Lake City, UT 84112, USA

[25] Department of Physics and JINA Center for the Evolution of the Elements, University of Notre Dame, Notre Dame, IN 46556, USA

[26] Cavendish Laboratory, University of Cambridge, 19 J. J. Thomson Avenue, Cambridge CB3 0HE, UK

[27] University of Cambridge, Kavli Institute for Cosmology, Cambridge, CB3 0HE, UK

[28] Department of Astronomy, University of Wisconsin-Madison, 475 N. Charter St., Madison WI 53706, USA

[29] Department of Physics and Astronomy, Vanderbilt University, 6301 Stevenson Center, Nashville, TN, 37235, USA

[30] Apache Point Observatory, P.O. Box 59, Sunspot, NM 88349, USA

[31] Department of Astronomy, New Mexico State University,

1. INTRODUCTION

The **S**loan **D**igital **S**ky **S**urvey (SDSS) has been observing the Universe using the 2.5-meter Sloan Foundation Telescope (Gunn et al. 2006) at **A**pache **P**oint **O**bservatory (APO) for over 15 years. The goal of the original survey (2000–2005; York et al. 2000) was to map large-scale structure with five-band imaging over $\sim \pi$ steradians of the sky and spectra of $\sim 10^6$ galaxies and $\sim 10^5$ quasars. This program was accomplished using a drift-scan camera (Gunn et al. 1998) and two fiber-fed optical R$\sim$1800 spectrographs (Smee et al. 2013), each with 320 fibers.

The imaging and spectroscopy goals were not entirely fulfilled in the initial five-year period, and thus SDSS-I was followed by SDSS-II (2005–2008; Abazajian et al. 2009). Its first goal was to complete the planned initial

Las Cruces, NM 88003, USA
[32] Sternberg Astronomical Institute, Moscow State University, Moscow 119992, Russia
[33] Observatories of the Carnegie Institution for Science, 813 Santa Barbara St, Pasadena, CA, 91101, USA
[34] Departamento de Astronomía, Universidad de Chile, Camino del Observatorio 1515, Las Condes, Santiago, Chile
[35] Centro de Astrofísica y Tecnologías Afines (CATA), Camino del Observatorio 1515, Las Condes, Santiago, Chile
[36] Center for Cosmology and Particle Physics, Department of Physics, New York University, New York, NY 10003, USA
[37] Aix Marseille Université, CNRS, LAM (Laboratoire d'Astrophysique de Marseille) UMR 7326, F-13388, Marseille, France
[38] National Optical Astronomy Observatory, 950 N Cherry Ave, Tucson, AZ 85719, USA
[39] Instituto de Física y Astronomía, Universidad de Valparaíso, Av. Gran Bretaña 1111, Playa, Ancha, Casilla 5030, Chile
[40] Millennium Institute of Astrophysics (MAS),Monseñor Sotero Sanz 100, oficina 104, Providencia, Santiago, Chile
[41] Department of Astronomy and Astrophysics, University of Toronto, 50 St. George Street, Toronto, ON, M55 3H4, Canada
[42] Dunlap Institute for Astronomy & Astrophysics, University of Toronto, 50 St. George Street, Toronto, Ontario, M5S 3H4, Canada
[43] Department of Astronomy and Astrophysics, Eberly College of Science, The Pennsylvania State University, 525 Davey Laboratory, University Park, PA 16802, USA
[44] Institute for Gravitation and the Cosmos, Pennsylvania State University, University Park, PA 16802, USA
[45] Department of Physics, The Pennsylvania State University, University Park, PA 16802, USA
[46] Kavli IPMU (WPI), UTIAS, The University of Tokyo, Kashiwa, Chiba 277-8583, Japan
[47] Departamento de Física Matemática, Instituto de Física, Universidade de São Paulo, CP 66318, CEP 05314-970, São Paulo, SP, Brazil
[48] Sub-department of Astrophysics, Department of Physics, University of Oxford, Denys Wilkinson Building, Keble Road, Oxford OX1 3RH, UK
[49] New York University Abu Dhabi, P.O. Box 129188, Abu Dhabi, United Arab Emirates
[50] Korea Institute for Advanced Study, 85 Hoegiro, Dongdaemun-gu, Seoul 130-722, Republic of Korea
[51] Departamento de Física, Centro de Ciências Naturais e Exatas, Universidade Federal de Santa Maria, 97105-900, Santa Maria, RS, Brazil
[52] Max-Planck-Institut für extraterrestrische Physik, Postfach 1312, Giessenbachstraße, 85741 Garching, Germany.
[53] Departamento de Astronomía, Universidad de Concepción, Casilla 160-C, Concepción, Chile
[54] Center for Astrophysics and Space Astronomy, Department of Astrophysical and Planetary Sciences, University of Colorado, 389 UCB, Boulder, CO 80309, USA
[55] Aix Marseille Université, CNRS/IN2P3, Centre de Physique des Particules de Marseille, UMR 7346, 13288, Marseille, France
[56] Department of Physics and Astronomy, Western Washington University, 516 High Street, Bellingham, WA 98225, USA
[57] Department of Physics and McWilliams Center for Cosmology, Carnegie Mellon University, 5000 Forbes Avenue, Pittsburgh, PA 15213, USA
[58] Observatório Nacional, 77 Rua General José Cristino, Rio de Janeiro, 20921-400, Brazil
[59] Department of Astronomy, University of Virginia, Charlottesville, VA 22904-4325, USA
[60] Department of Physics, Geology, and Engineering Tech, Northern Kentucky University, Highland Heights, KY 41099, USA
[61] Laboratoire d'Astrophysique, École Polytechnique Fédérale de Lausanne, 1015 Lausanne, Switzerland
[62] Centro de Investigaciones de Astronomía, AP 264, Mérida 5101-A, Venezuela
[63] McDonald Observatory, The University of Texas at Austin, 1 University Station, Austin, TX 78712, USA
[64] Tsinghua Center for Astrophysics and Department of Physics, Tsinghua University, Beijing 100084, P. R. China
[65] Harvard-Smithsonian Center for Astrophysics, 60 Garden St., MS 20, Cambridge, MA 02138, USA
[66] School of Physics and Astronomy, University of Birmingham, Edgbaston, Birmingham B15 2TT, UK
[67] Stellar Astrophysics Centre, Department of Physics and Astronomy, Aarhus University, Ny Munkegade 120, DK-8000 Aarhus C, Denmark
[68] European Southern Observatory, Karl-Schwarzschild-Str. 2, 85748 Garching, Germany
[69] Université Lyon 1, Observatoire de Lyon, Centre de Recherche Astrophysique de Lyon and École Normale Supérieure de Lyon, 9 avenue Charles André, F-69230 Saint-Genis Laval, France
[70] Steward Observatory, University of Arizona, 933 North Cherry Avenue, Tucson, AZ 85721, USA
[71] Institut UTINAM, CNRS-UMR6213, OSU THETA, Université Bourgogne-Franche-Comté, 41bis avenue de l'Observatoire, 25010 Besançon Cedex, France
[72] Space Telescope Science Institute, 3700 San Martin Drive, Baltimore, MD 21218, USA
[73] CSRA, Inc., 3700 San Martin Drive, Baltimore, MD 21218, USA
[74] Department of Physics & Astronomy, University of Iowa, Iowa City, IA 52245
[75] Laboratoire AIM, CEA/DRF – CNRS - Univ. Paris Diderot – IRFU/SAp, Centre de Saclay, 91191 Gif-sur-Yvette Cedex, France
[76] National Astronomy Observatories, Chinese Academy of Science, 20A Datun Road, Chaoyang District, Beijing, 100012, P. R. China
[77] Sorbonne Universités, UPMC Univ Paris 06, UMR 7095, Institut d'Astrophysique de Paris, 98 bis boulevard Arago, F-75014, Paris, France
[78] Laboratoire de Physique Nucléaire et de Hautes Energies, Université Pierre et Marie Curie, 4 Place Jussieu,75005 Paris, France
[79] Osservatorio Astronomico di Padova – INAF, Vicolo dell'Osservatorio 5, I-35122, Padova, Italy
[80] Institute of Cosmology & Gravitation, University of Portsmouth, Dennis Sciama Building, Portsmouth, PO1 3FX, UK
[81] DePauw University, Greencastle, IN 46135, USA
[82] LPNHE, CNRS/IN2P3, Université Pierre et Marie Curie Paris 6, Université Denis Diderot Paris 7, 4 place Jussieu, 75252 Paris CEDEX, France
[83] Department of Astronomy, Case Western Reserve University, Cleveland, OH 44106, USA
[84] Max Planck Institute for Solar System Research,Justus-von-Liebig-Weg 3, 37077 Goettingen, Germany
[85] Sydney Institute for Astronomy (SIfA), School of Physics, University of Sydney, NSW 2006, Australia
[86] SETI Institute, 189 Bernardo Avenue, Mountain View, CA 94043, USA
[87] Rice University, 6100 Main St, Houston, TX 77005, USA
[88] Department of Astronomy, The Ohio State University, 140 W. 18th Ave., Columbus, OH 43210, USA
[89] Center for Cosmology and AstroParticle Physics, The Ohio State University, 191 W. Woodruff Ave., Columbus, OH 43210,

large scale structure redshift survey as the Legacy program. It added SEGUE (**S**loan **E**xtension for **G**alactic **U**nderstanding and **E**xploration; Yanny et al. 2009), a spectroscopic survey focused on stars, and imaged an average of once every five days a $\sim$ 200 sq. deg area along the celestial equator with repeated scans in SDSS-I ("Stripe 82"), to search for Type Ia supernovae and other transients (Frieman et al. 2008).

The success of SDSS as a cosmological probe, particularly the detection of the clustering of luminous red galaxies (LRG) on the 100 h^{-1} Mpc scale expected from baryon acoustic oscillations (BAO; Eisenstein et al. 2005), led to the conception and implementation of BOSS (**B**aryon **O**scillation **S**pectroscopic **S**urvey; Dawson et al. 2013) as the flagship program in the third version of the survey, SDSS-III (2008–2014; Eisenstein et al. 2011). As part of BOSS, SDSS-III imaged additional areas in the part of the south Galactic cap visible from the Northern hemisphere. At the conclusion of these observations, the SDSS imaging camera was retired and is now part of the permanent collection of the Smithsonian National Air and Space Museum[126]. During the summer shutdown in 2009, the original SDSS spectrographs were replaced by new, more efficient, spectrographs to be used by BOSS. The BOSS spectrographs featured expanded wavelength coverage (3560Å$<\lambda<$10400 Å), new CCD detectors with improved read noise, smaller pixels (15μm), and improved quantum efficiency, and VPH gratings instead of the original replicated surface relief gratings (Smee et al. 2013). The two spectrographs were now fed by 500 fibers each so that the desired number of redshifts could be reached in the planned survey lifetime.

During the first year of SDSS-III (2008–2009), the SEGUE-2 survey (Rockosi et al., in preparation) used the original SDSS spectrographs to observe additional Milky Way halo fields to target distant halo samplers and trace substructure. In SDSS-III all bright time could be used for scientific observations with the arrival of two new instruments. MARVELS (**M**ulti-object **APO** **R**adial **V**elocity **E**xoplanet **L**arge-area **S**urvey; Paegert et al. 2015; Thomas et al. 2016) used a novel multiplexing interferometer to observe 60 stars simultaneously to search for radial velocity variations caused by hot Jupiters and close brown dwarf companions. APOGEE (**A**pache **P**oint **O**bservatory **G**alactic **E**volution *E*xperiment; Majewski et al. 2015) used a 300-fiber, R$\sim$22,000 H-band spectrograph (Majewski et al. 2015; Wilson et al., in preparation) to measure stellar parameters, chemical abundances, and radial velocities, mainly for red giants (Zasowski et al. 2013).

Since routine operations started in 2000, there have been thirteen public data releases. All data releases are cumulative, re-releasing the best reduction of all previously taken data. The most recent of these was Data Release 12 (Alam et al. 2015), which contained all of the SDSS-III data, as well as the re-reduced data from SDSS-I and SDSS-II. SDSS-I to SDSS-III imaged 14,555 degree^2 in the five filters (Fukugita et al. 1996; Doi et al. 2010). Most of the sky was surveyed once or twice, but regions in Stripe 82 were observed between 70 and 90 times. By the time of their retirement, the SDSS spectrographs had obtained R$\sim$1800 optical spectra for 860,836 galaxies, 116,003 quasars, and 521,990

USA
[90] Max-Planck-Institut für Astrophysik, Karl-Schwarzschild-Str. 1, D-85748 Garching, Germany
[91] Institute for Astronomy, University of Vienna, Türkenschanzstrasse 17, 1180 Vienna, Austria
[92] Department of Physics and Astronomy, University of California, Irvine, Irvine, CA 92697, USA
[93] Instituto de Astrofísica, Pontificia Universidad Católica de Chile, Av. Vicuna Mackenna 4860, 782-0436 Macul, Santiago, Chile
[94] Academia Sinica Institute of Astronomy and Astrophysics, P.O. Box 23-141, Taipei 10617, Taiwan
[95] Astrophysics Research Institute, Liverpool John Moores University, IC2, Liverpool Science Park, 146 Brownlow Hill, Liverpool L3 5RF, UK
[96] Instituto de Física, Universidade Federal do Rio Grande do Sul, Campus do Vale, Porto Alegre, RS, , 91501-907, Brazil
[97] CSIC, Serrano, 117 - 28006, Madrid, Spain
[98] Space Science Institute, 4750 Walnut Street, Suite 205, Boulder, CO 80301, USA
[99] ELTE Gothard Astrophysical Observatory, H-9704 Szombathely, Szent Imre herceg st. 112, Hungary
[100] Departamento de Ciencias Fisicas, Universidad Andres Bello, Sazie 2212, Santiago, Chile
[101] Max-Planck-Institut für Astronomie, Konigstuhl 17, D-69117 Heidelberg, Germany
[102] LESIA, UMR 8109, Université Pierre et Marie Curie, Université Denis Diderot, Observatoire de Paris, F-92195 Meudon Cedex, France
[103] Department of Physics and Astronomy, University of Wyoming, Laramie, WY 82071, USA
[104] Department of Physics and Astronomy, University of Alabama, Tuscaloosa, AL 35487-0324, USA
[105] Institute for Astronomy, University of Edinburgh, Royal Observatory, Edinburgh EH9 3HJ, UK
[106] Université Paris 6 et CNRS, Institut d'Astrophysique de Paris, 98bis blvd. Arago, 75014 Paris, France
[107] Instituto de Astrofísica de Andalucía (CSIC), Glorieta de la Astronomía, E-18080 Granada, Spain
[108] Department of Astrnonomy and Astrophysics, University of California, Santa Cruz and UC Observatories, Santa Cruz, CA, 95064, USA
[109] Dipartimento di Fisica e Astronomia, Università di Padova, Vicolo dell'Osservatorio 2, I-35122 Padova, Italy
[110] Instituto de Astronomía, Universidad Nacional Autónoma de México, Unidad Académica en Ensenada, Ensenada BC 22860, Mexico
[111] Department of Astronomy and Space Science, Sejong University, Seoul 143-747, Korea
[112] Hubble Fellow
[113] Observatoire de la Côte d'Azur, Laboratoire Lagrange, 06304 Nice Cedex 4, France
[114] Department of Physics and Astronomy, Ohio University, Clippinger Labs, Athens, OH 45701, USA
[115] Institute of Space Sciences (IEEC-CSIC), Carrer de Can Magrans, E-08193, Barcelona, Spain
[116] University of Texas at Austin, McDonald Observatory, McDonald Observatory, TX, 79734, USA
[117] Brookhaven National Laboratory, Upton, NY 11973, USA
[118] National Optical Astronomy Observatories, Tucson, AZ, 85719, USA
[119] School of Physics, The University of New South Wales, Sydney NSW 2052, Australia
[120] Department of Astrophysical Sciences, Princeton University, Princeton, NJ 08544, USA
[121] Instituto de Física, Universidad Nacional Autónoma de México, Apdo. Postal 20-364, Mexico
[122] Department of Physical Sciences, The Open University, Milton Keynes MK7 6AA, UK
[123] Physics Department, Austin College, Sherman, TX 75092, USA
[124] Department of Physics and Astronomy, University of Kentucky, 505 Rose Street, Lexington, KY 40506, USA
[125] Department of Physics, Bridgewater College, 402 E College St., Bridgewater, VA 22812, USA

[126] `https://airandspace.si.edu/collection-objects/camera-imaging-digital-sloan-digital-sky-survey-ccd-array`

stars. With the BOSS spectrographs, the survey has added data with similar resolution for 1,372,737 galaxies, 294,512 quasars, and 247,216 stars. APOGEE has contributed high-resolution IR spectra of 156,593 stars. MARVELS had observed 3233 stars with at least 16 epochs of radial velocity measurements.

The success of the previous Sloan Digital Sky Surveys and the continuing importance of the wide-field, multiplexing capability of the Sloan Foundation Telescope motivated the organization of the fourth phase of the survey, SDSS-IV (Blanton et al., in preparation). SDSS-IV extends SDSS observations to many fibers covering the spatial extent of nearby galaxies, to new redshift regimes, and to the parts of the Milky Way and dwarf galaxies that are only visible from the Southern Hemisphere. The MaNGA (**Ma**pping **N**earby **G**alaxies at **A**PO) survey studies galaxy formation and evolution across a wide range of masses and morphological types by observing a substantial portion of the optical spatial extent of $\sim 10^4$ galaxies (Bundy et al. 2015). It accomplishes this goal by employing 17 bundles ranging in size between 19 and 127 fibers to cover targets selected from an extended version of the NASA-Sloan Atlas[127] and 12 bundles of 7 fibers for calibration stars. These integral field units (IFUs) feed the BOSS spectrographs, providing information on the properties of gas and stars in galaxies out to 1.5–2.5 effective radii (R_e).

Another survey, eBOSS (**e**xtended **B**aryon **O**scillation **S**pectroscopic **S**urvey Dawson et al. 2016), shares the dark time equally with MaNGA. eBOSS will measure with percent-level precision the distance-redshift relation with BAO in the clustering of matter over the relatively unconstrained redshift range $0.6 < z < 2.2$. This redshift range probes the Universe during its transition from matter-dominated to dark-energy-dominated. Multiple measurements of the angular diameter distance ($d_A(z)$) and Hubble parameter ($H(z)$) from BAO over the redshifts covered by eBOSS are therefore crucial for understanding the nature of dark energy. eBOSS will use spectroscopic redshifts from more than 400,000 LRGs and nearly 200,000 Emission-Line Galaxies (ELGs) to extend the final BOSS galaxy clustering measurements (Alam et al. 2016) by providing two new BAO distance measurements over the redshift interval $0.6 < z < 1.1$ Roughly 500,000 spectroscopically-confirmed quasars will be used as tracers of the underlying matter density field at $0.9 < z < 2.2$, providing the first measurements of BAO in this redshift interval. Finally, the Lyman-α forest imprinted on approximately 120,000 new quasar spectra will give eBOSS an improved BAO measurement over that achieved by BOSS (Delubac et al. 2015; Bautista, et al., in preparation) The three new tracers will provide BAO distance measurements with a precision of 1% at $z = 0.7$ (LRG), 2% at $z = 0.85$ (ELG), and 2% at $z = 1.5$ (quasar) while the enhanced Lyman-α forest sample will improve BOSS constraints by a factor of 1.4. Furthermore, the clustering from eBOSS tracers will allow new measurements of redshift-space distortions (RSD), non-Gaussianity in the primordial density field, and the summed mass of neutrino species. Extensively observing these redshift ranges for the first time in SDSS required re-evaluation of targeting strategies. Preliminary targeting schemes for many of these classes of objects were tested as part of SEQUELS (*S*loan *E*xtended *QU*asar, *E*mission-line galaxy, *L*uminous red galaxy *S*urvey), which used 126 plates observed across SDSS-III and -IV. DR13 includes all SEQUELS data, giving the largest SDSS sample to date of spectra targeting intermediate redshift ranges. SDSS-IV also allocated a significant number of fibers on the eBOSS plates to two additional dark-time programs. TDSS(*T*ime *D*omain *S*pectroscopic *S*urvey; Morganson et al. 2015) seeks to understand the nature of celestial variables by deliberately targeting objects that vary in combined SDSS DR9 and Pan-STARRS1 data (PS1; Kaiser et al. 2002) . A large number of the likely quasar targets so selected are also targeted by the main eBOSS algorithms and therefore meet the goals of both surveys. TDSS-only targets fill $\sim$ 10 spectra per square degree. The main goal of the SPIDERS (**Sp**ectroscopic **Id**entification of **eR**OSITA **S**ources) survey is to characterize a subset of X-ray sources identified by eROSITA (**e**xtended **Ro**entgen **S**urvey with an **I**maging **T**elescope **A**rray; Predehl et al. 2014) . Until the first catalog of eROSITA sources is available, SPIDERS will target sources from the RASS (**Ro**etgen **A**ll **S**ky **S**urvey; Voges et al. 1999) and XMM (**X**-ray **M**ulti-mirror **M**ission; Jansen et al. 2001). SPIDERS will also obtain on average $\sim$ 10 spectra per square degree over the course of SDSS-IV, but the number of fibers per square degree on a plate is weighted toward the later years to take advantage of the new data from eROSITA.

In bright time at APO, APOGEE-2, the successor to APOGEE (hereafter APOGEE-1) in SDSS-IV, will continue its survey of the Milky Way stellar populations. Critical areas of the Galaxy, however, cannot be observed from APO, including the more distant half of the Galactic bar, the fourth quadrant of the disk, and important dwarf satellites of the Milky Way, such as the Magellanic Clouds and some dwarf spheroidals. SDSS-IV will for the first time include operations outside of APO as the result of Carnegie Observatories and the Chilean Participation Group joining the collaboration. A second APOGEE spectrograph is being constructed for installation on the 2.5-meter du Pont Telescope (Bowen & Vaughan 1973) at Las Campanas Observatory (LCO) near La Serena, Chile. When APOGEE-2S begins survey operations in 2017, approximately 300 survey nights on the du Pont Telescope will be used to extend the APOGEE-2 survey to the Southern Hemisphere.

Data Release 13 (DR13) is the first data release for SDSS-IV, which will have regular public, documented data releases, in keeping with the philosophy of SDSS since its inception. In this paper, we describe the data available in DR13, focusing on the data appearing here for the first time. We present overall descriptions of the sample sizes and targeting and provide a detailed bibliography of the technical papers available to understand the data and the surveys in more detail. These technical papers and the SDSS website (`www.sdss.org`) contain critical information about these data, which here is only summarized.

2. SCOPE OF DATA RELEASE 13

SDSS-IV has been operating since July 2014. DR13 contains data gathered between July 2014 and July 2015

---

[127] `http://www.nsatlas.org`

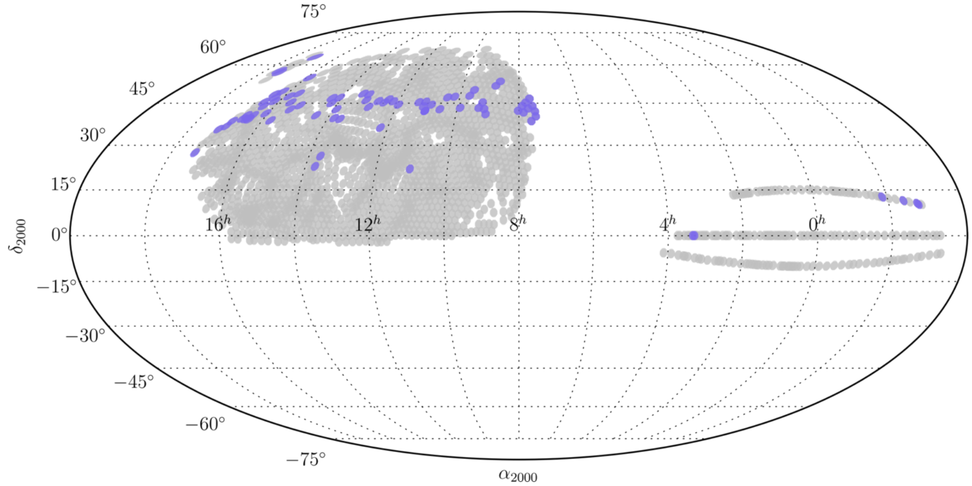

Fig. 1.— In grey are shown the locations in equatorial coordinates of all possible plates with MaNGA galaxies, each containing 17 galaxy targets. Because the MaNGA targets are selected to have SDSS photometry, this footprint corresponds to the Data Release 7 imaging data (Abazajian et al. 2009). Approximately 30% of these will be observed in the full planned MaNGA survey. The blue shows the plates observed in the first year of MaNGA for which data cubes are released in this paper.

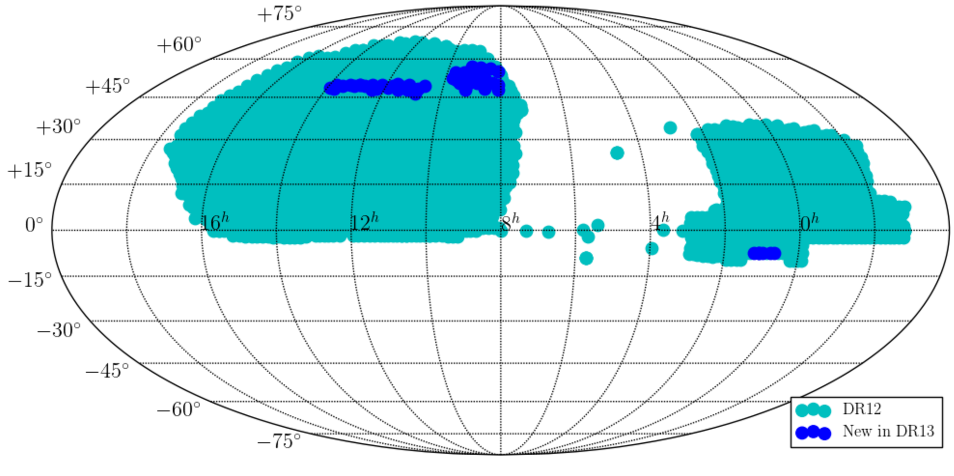

Fig. 2.— Coverage of DR13 data from BOSS and SEQUELS in equatorial coordinates. The blue areas show the locations in equatorial coordinates of the five new BOSS plates (SGC) and the 126 SEQUELS plates (NGC) released in DR13. The green represents the area covered by BOSS in DR12. The SEQUELS plates released in DR12 lie in the same region as the new ones in DR13, providing complete coverage over roughly 400 square degrees.

and is summarized in Table 1. The categories under MaNGA galaxies are described in §5. The SEQUELS targeting flags are listed and described in Alam et al. (2015). Figures 1, 2, 3 show the sky coverage of the MaNGA, eBOSS and APOGEE-2 surveys respectively. In the subsequent sections, we discuss each survey's data in detail, but briefly DR13 includes

- Reduced data for the 82 MaNGA galaxy survey plates, yielding 1390 reconstructed 3-D data cubes for 1351 unique galaxies, that were completed by July 2015. Row-stacked spectra (RSS) and raw data are also included.
- Reduced BOSS spectrograph data for an additional 60 SEQUELS plates, completing the SEQUELS program. The total number of SEQUELS plates released in DR12 and DR13 is 126. These plates provide a complete footprint covering roughly 400 square degrees that will not be revisited in eBOSS. The targets include a superset of the eBOSS LRG and quasar samples, a sample of variability-selected point sources at a much higher density than in TDSS, and new X-ray-selected objects selected by similar criteria to targets in SPIDERS.
- The reduced data for five BOSS plates at low declination in the SGC. These plates were drilled during SDSS-III but not observed due to insufficient open-dome time when they were observable. The plates were observed early in SDSS-IV to fill in the footprint in this region.
- Spectroscopic data from BOSS processed with a new version of the data reduction pipeline, which results in less-biased flux values.
- All APOGEE-1 data re-reduced with improved telluric subtraction and analyzed with an improved pipeline and synthetic grid, including adding rotationally broadening as a parameter for dwarf spectra.
- New species (C I, P, Ti II, Co, Cu, Ge, and Rb) with reported abundances for APOGEE-1 sample.
- Stellar parameters for APOGEE-1 stars with cooler effective temperatures ($T_{\rm eff} < 3500$K), derived by an extension of the grid of synthetic spectra using MARCS (Gustafsson et al. 2008) model atmospheres.
- Recalibrated SDSS imaging catalogs, using the hypercalibration to PanSTARRS-1 implemented by Finkbeiner et al. (2016).
- Valued-added catalogs, see Table 2. More detail and direct links to the catalogs and their datamodels can be found at `http:\www.sdss.org/dr13/data_access/vac`.
- The most recent reductions of all data from previous iterations of SDSS is included as a matter of course. For MARVELS data, these data are the same as in DR12; for SEGUE and SEGUE-2, the same as in DR9.

DR13 contains only a subset of the reduced or raw data for all surveys taken between July 2014 and July 2015. The first *two* years of eBOSS data are needed before useful cosmological constraints can be extracted. APOGEE-2 is using the first year of SDSS-IV data to work on science verification and targeting optimization for new classes of targets and new survey strategies. Both of these surveys will release more extensive new data in Data Release 14.

3. DATA DISTRIBUTION

The data for DR13 are distributed through the same mechanisms available in DR12, with some significant changes to the environment used to access the catalog data (see below). Raw and processed image and spectroscopic data are available, as before, through the Science Archive Server (SAS, `data.sdss.org/sas/dr13`), and also for imaging data, optical spectra, and APOGEE IR spectra through an interactive web application (`dr13.sdss.org`, available soon). The catalogs of photometric, spectroscopic, and derived quantities are available through the Catalog Archive Server or CAS (Thakar et al. 2008; Thakar 2008) via two primary modes of access: browser-based queries of the database are available through the SkyServer Web application (`http://skyserver.sdss.org`) in synchronous mode, and more advanced and extensive querying capabilities are available through CasJobs (`http://skyserver.sdss.org/casjobs`) in asynchronous or batch mode that allows time-consuming queries to be run in the background (Li & Thakar 2008).

The CAS is now part of the new SciServer (http://www.sciserver.org/) collaborative science framework that allows users single-sign-on access to a suite of collaborative data-driven science services that includes the classic SDSS services of SkyServer and CasJobs. These services are essentially unchanged in their user interfaces but have acquired powerful new capabilities and undergone fundamental re-engineering to make them interoperable and applicable to other science domains. New services are also available to users once they register on the SciServer portal, and these services work seamlessly with the existing tools. Most notable among the new offerings are SciDrive, a distributed DropBox-like file store; SkyQuery, a federated cross-matching service that compares and combines data from a collection (federation) of multi-wavelength archives (SkyNodes); and SciServer Compute, a powerful new system for uploading complex analysis scripts as Jupyter notebooks (using Python, MatLab or R) running in Docker containers.

Links to all of these methods are provided at the SDSS website (`http://www.sdss.org/dr13/data_access`) The data processing software for APOGEE, BOSS, and SEGUE are publicly available at `http://www.sdss.org/dr13/software/products`. A set of tutorial examples for accessing SDSS data is provided at `http://www.sdss.org/dr13/tutorials`. All flat files are available for download at `http://data.sdss.org/datamodel/`

4. RECALIBRATION OF IMAGING DATA

DR13 includes a photometric recalibration of the SDSS imaging data. Using the PS1 photometric calibrations of Schlafly et al. (2012), Finkbeiner et al. (2016) have red-

TABLE 1
Reduced spectroscopic data in DR13

Target Category	# DR12	# DR12+13
MaNGA main galaxy sample:		
`PRIMARY_v1_2`	0	600
`SECONDARY_v1_2`	0	473
`COLOR-ENHANCED_v1_2`	0	216
MaNGA ancillary galaxies[1]	0	31
MaNGA Other	0	62
SEQUELS		
`LRG_IZW`	11781	21271
`LRG_RIW`	11691	20967
`QSO_EBOSS_CORE`	19455	33367
`QSO_PTF`	13227	22609
`QSO_REOBS`	1357	2238
`QSO_EBOSS_KDE`	11836	20474
`QSO_EBOSS_FIRST`	293	519
`QSO_BAD_BOSS`	59	95
`QSO_BOSS_TARGET`	59	95
`DR9_CALIB_TARGET`	28594	49765
`SPIDERS_RASS_AGN`	162	275
`SPIDERS_RASS_CLUS`	1533	2844
`TDSS_A`	9412	17394
`TDSS_FES_DE`	40	70
`TDSS_FES_DWARFC`	19	29
`TDSS_FES_NQHISN`	73	148
`TDSS_FES_MGII`	1	2
`TDSS_FES_VARBAL`	55	103
`SEQUELS_PTF_VARIABLE`	700	1153
APOGEE-2		
All Stars	164562	164562
NMSU 1-meter stars	894	894
Telluric stars	17293	17293
Commissioning stars	11917	11917

[1] Many MaNGA ancillary targets were also targeted as part of the main galaxy sample, and are counted twice in this table.

TABLE 2
Value-Added Catalogs New in DR13

Catalog Description	Reference	`http://data.sdss.org/sas/dr13/`
SPIDERS Clusters demonstration sample catalog	Clerc et al. (2016, in prep.)	`eboss/spiders/analysis/`
SPIDERS AGN target selection catalog	Dwelly et al (2016, in prep.)	`eboss/spiders/target/`
SPIDERS cluster target selection catalog	Clerc et al. (2016, in prep.)	`eboss/spiders/target/`
WISE Forced Photometry	Lang et al. (2016)	`eboss/photoObj/external/WISEForcedTarget/301/`
Composite Spectra of Emission-line Galaxies	Zhu et al. (2015)	`eboss/elg/composite/v1_0/`
ELG Fisher selection catalog	Delubac et al, (2016, in prep)	`eboss/target/elg/fisher-selection/`
Redmonster redshift & spectral classification catalog	Hutchinson et al. (2016, in prep)	`eboss/spectro/redux/redmonster/v5_9_0/v1_0_1/`
QSO Variability	Palanque-Delabrouille et al. (2016)	`eboss/qso/variability/`
APOGEE DR13 red-clump catalog	Bovy et al. (2014)	`apogee/vac/apogee-rc/cat/`

erived the g, r, i and z band zero points and the flat fields in all five bands (including u). The residual systematics are reduced to 0.9, 0.7, 0.7 and 0.8% in the $griz$ bands, respectively; several previously uncertain calibrations of specific runs are also now much better constrained. The resulting recalibrated imaging catalogs are the basis for the eBOSS and MaNGA targeting.

For the MaNGA target selection, we are using the NASA-Sloan Atlas (NSA; Blanton et al. 2011), a reanalysis of the SDSS photometric data using sky subtraction and deblending better tuned for large galaxies. Relative to the originally distributed version of that catalog, we have used the new calibrations mentioned above, increased the redshift range up to $z = 0.15$, and have added an elliptical aperture Petrosian measurement of flux, which MaNGA targeting is based upon. DR13 includes the NSA catalog (version `v1_0_1`) associated with this reanalysis as the `nsatlas` CAS table and as a file on the SAS. For the MaNGA galaxies released in DR13, we provide the actual images (referred to in MaNGA documentation as "preimaging") on the SAS as well.

Lang et al. (2016) reanalyzed data from the **W**ide-field **I**nfrared **S**atellite **E**xplorer (WISE; Wright et al. 2010) to use for eBOSS targeting. They used positions and galaxy profile measurements from SDSS photometry as input structural models and constrained fluxes in the WISE 3.4 μm and 4.6 μm bands. These results agree with the standard WISE reductions to within 0.03 mag for high signal-to-noise ratio, isolated point sources in WISE. However, the new reductions provide flux measurements

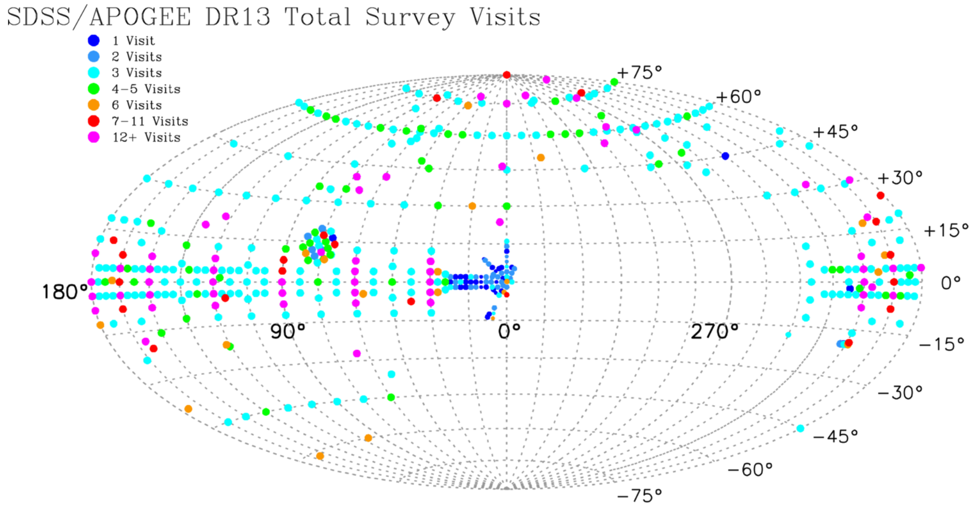

Fig. 3.— Coverage of APOGEE-2 DR13 data in Galactic coordinates; the raw data and its coverage is the same as in DR12, but it has been reprocessed through the latest reduction pipeline and ASPCAP versions. The color coding denotes the number of visits to each field, as indicated in the legend.

for low signal-to-noise ratio ($< 5\sigma$) objects detected in the SDSS but not in WISE (over 200 million objects). Despite the fact that the objects are undetected, their flux measurements are nevertheless informative for target selection, in particular for distinguishing stars from quasars. This photometry is provided as a value-added catalog in the `wiseForcedTarget` CAS table and on the SAS as described in Table 2.

The Galactic extinction estimates published in the SDSS imaging tables (`photoObj` and related tables in the CAS) have been changed. The Galactic extinction still uses the Schlegel et al. (1998) models of dust absorption to estimate $E(B-V)$, but the Galactic extinction coefficients for each band have been updated as recommended by Schlafly & Finkbeiner (2011). The extinction coefficients R_u, R_g, R_r, R_i, and R_z are changed from the values used in BOSS (5.155, 3.793, 2.751, 2.086, 1.479) to updated values (4.239, 3.303, 2.285, 1.698, 1.263). The corresponding numbers for the WISE bands are $R_{W1} = 0.184$ for the WISE 3.4μm band and $R_{W2} = 0.113$ for the 4.6μm band (Fitzpatrick 1999).

5. MANGA: INTEGRAL FIELD SPECTROSCOPIC DATA

MaNGA is investigating the internal kinematics and composition of gas and stars in low redshift ($z \leq 0.15$) galaxies using fiber bundles to feed the BOSS spectrographs. Bundy et al. (2015) describe the high-level scientific goals, scope, and context of the survey in investigating galaxy formation while Yan et al. (2016b) give a detailed description of the survey design, execution, and data quality relevant to DR13. With nearly 1390 data cubes released, MaNGA's DR13 data products represent the largest public sample, by more than a factor of 2, of galaxies observed with integral field spectroscopy. This data set signifies a valuable first step in MaNGA's goals to reveal the internal properties and dynamics of a statistically powerful sample of galaxies, that spans a broad range in stellar mass, local environment, morphology, and star formation history. Individual observations across the sample are of sufficient quality to characterize the spatially-dependent composition of stars and gas as well as their internal kinematics, thus providing important clues on growth and star formation fueling, the build-up of spheroidal components, the cessation of star formation, and the intertwined assembly history of galaxy subcomponents.

The survey was made possible through an instrumentation initiative in SDSS-IV to develop a reliable and efficient way of bundling 1423 optical fibers into tightly-packed arrays that constitute MaNGA's IFUs (Drory et al. 2015). For each pointing, MaNGA observes 17 science targets with IFUs ranging from 19 to 127 fibers (with diameters of 12−32″). The IFU size distribution was optimized in concert with the sample design (Wake et al., in preparation) which targets SDSS-I/II main sample galaxies at a median redshift of 0.03 to obtain in 6 years a sample of 10^4 galaxies with uniform radial coverage and a roughly flat distribution in $\log \mathrm{M}_*$ limited to $\mathrm{M}_* > 10^9 \mathrm{M}_\odot$. Careful attention was paid to optimizing hardware and an observing strategy that ensures high quality imaging spectroscopy (Law et al. 2015) and to surface photometric flux calibration with a precision better than 5% across a majority of the wavelength range, 3,622-10,354Å(Yan et al. 2016a). As described in these papers, salient aspects included protocols for constraining hour-angles of observations to limit differential atmospheric diffraction, dithering exposures to avoid gaps in the coverage of the targets because of space between the fibers, and special calibration mini-bundles to ensure reliable absolute and relative flux calibration. An automated pipeline delivers sky-subtracted, flux-calibrated row-stacked-spectra (RSS) and datacubes for all sources (Law et al. 2016).

5.1. *MaNGA DR13 Main Galaxy Sample*

At the completion of SDSS-IV, the MaNGA survey's main galaxy sample will include $\sim 10^4$ galaxies with $\mathrm{M}_* > 10^9 \mathrm{M}_\odot$ and a roughly flat stellar mass distribution. DR13's 1390 galaxy data cubes, corresponding to 1351 unique galaxies makes it the largest public sample of galaxies with IFU spectroscopy. MaNGA's main galaxy sample consists of three major parts: Primary sample, Secondary sample, and the Color-Enhanced supplement.

The Primary sample and the Secondary sample are selected from two luminosity-dependent redshift bands, as shown in Figure 4. The selection for each sample is volume-limited at each absolute i-band magnitude. The shape of the redshift bands is motivated by MaNGA's science requirements of having a uniform spatial *coverage* in units of galaxy's effective radius R_e and having a roughly flat stellar mass distribution (Yan et al. 2016b, ;Wake et al., in prep). Figure 5 shows the distribution of the MaNGA DR13 galaxies in the stellar mass vs. dark matter halo mass plane. Because more massive galaxies are on average larger, we observe them at a larger distance than low mass galaxies. We chose the redshift bands so that the great majority of the Primary (Secondary) sample is covered by our fiber bundles to 1.5 R_e (2.5 R_e) along their major axes. This has the commensurate effect of changing the physical resolution systematically as a function of stellar mass, as illustrated in Figure 4. Potential deleterious effects of this change in sampling are addressed by an ancillary program, described below.

We also designed a Color-Enhanced supplement, as a supplement to the Primary sample, to enhance the sampling of galaxies with rare color-magnitude combinations, such as low-mass red galaxies, high mass blue galaxies, and green valley galaxies. This is achieved by extending the redshift limits around the Primary sample redshift band for each underpopulated region in color-magnitude space.

The combination of the Primary sample and the Color-Enhanced supplement is referred to as the Primary+ sample. We provide in our data release the redshift limits over which each galaxy is selected. This permits a correction to the sample using $1/V_{\max}$ weight to reconstruct a volume-limited representation of the galaxy population. More details of how we arrived at this selection can be found in Yan et al. (2016b) and Wake et al. (in prep). Wake et al. (in prep) provides the details of how to properly weight the sample to reconstruct a volume-limited representation.

Among the 1351 unique galaxies released in DR13, there are 600 Primary Sample galaxies, 473 Secondary Sample galaxies, and 216 Color-Enhanced supplement galaxies. There are 62 galaxies that do not belong to any of the above. Some of these are ancillary program targets (see below), some are filler objects on plates with spare bundles, and others are galaxies selected using older, obsolete versions of the selection and observed on early plates. For most statistical analyses, these 62 galaxies should be excluded.

Which sample a given target galaxy belongs to is given by the MANGA_TARGET1 bitmask (or mngtarg1 in the "drpall" file; see §5.2). Primary sample galaxies have bit 10 set to 1, Secondary Sample galaxies have bit 11 set to 1, and Color-Enhanced Supplement Galaxies have bit 12 set to 1. Bits 1-9 are for obsolete selections and should be ignored.

5.1.1. *MaNGA Galaxy Ancillary Programs*

Roughly 5% of the IFUs are assigned to ancillary science programs defined by and allocated through internal competition and review. This assignment takes advantage of sky regions with a low density of galaxies defined by our main survey criteria (above) or where certain rare classes of objects, possibly outside our selection cuts, are of sufficiently high science value to re-allocate IFUs from the main program. Such high-value targets sometimes come from the main sample, but the ancillary science goals require a different bundle size, a slightly different center positions, or higher prioritization over the random selection among the main sample galaxies. There are also science cases where using observing strategies different from standard MaNGA observations are required. These lead to dedicated plates.

We solicited ancillary proposals in all these categories during the first year of survey observations, and they started to be included in plate design half way through this year. Consequently, the ancillary fraction in DR13 is smaller than 5%. Some ancillary programs have tens of targets approved but only a few got observed during the first year, while some have no observations during this period. More targets for these programs will be observed in the future. To identify ancillary targets, one should use the MANGA_TARGET3 bitmask (or mngtarg3 in the drpall file). All ancillary targets have MANGA_TARGET3 greater than zero. Additional information on the scientific justification and targeting for each ancillary program can be found at `http://www.sdss.org/dr13/managa/manga-target-selection/ancillary-targets`. Here we provide some highlights and the corresponding bitnames.

- *Luminous AGN:* This program increases the number of host galaxies of the most luminous active galactic nuclei (AGN). The first source of targets is the BAT 70-month Hard X-ray catalog (Baumgartner et al. 2013). These have the bitname `AGN_BAT`. To increase the sample size further we used the [OIII]-selected catalog of Mullaney et al. (2013) (bitname `AGN_OIII`). To match the distribution of bolometric luminosities between the samples, we selected 5 [OIII] objects at comparable $L_{\rm bol}$ to each BAT object, within a redshift range of 0.01-0.08. The bolometric corrections are from Shao et al. (2013) and Vasudevan & Fabian (2009).

- *Edge-On Starbursts:* We will use edge-on starbursts to study the morphology and ionization state of large-scale outflows. To identify good targets, the specific star formation rate (sSFR) and inclination of every object in the baseline MaNGA targeting catalog was calculated. The sSFR was determined using WISE photometry from Lang et al. (2016) and the calibration between the W4 filter and 22 μm emission in Jarrett et al. (2013) . We then use a calibration from Cluver et al. (2014) to derive the sSFR. The axis ratio `SERSIC_BA` in the targeting catalog was used to derive the inclination. All targets in this program have log sSFR> -8.75 and inclination > 75 deg.. The four galaxies in DR13 that have these properties, but were not included in the main galaxy target sample, have bitname `EDGE_ON_WINDS`.

- *Close Pairs and Mergers:* Interactions and mergers can play a key role in galaxy evolution, and therefore an ancillary program was accepted that either slightly adjusted the field centers for some targets already included in the main galaxy sample or placed new IFUs on galaxies. Close pairs are defined as galaxies in the NSA catalog or the SDSS group catalog of Yang et al. (2007) and X. Yang (private communication) with projected separation < 50 kpc h^{-1} and line-of-sight velocity (dV) < 500 km s^{-1}, if both redshifts are available. If the bitname is `PAIR_ENLARGE`, then to get the full pair required a larger IFU than the one originally scheduled by the targeting algorithm (Wake et al, in prep). If the bitname is `PAIR_RECENTER` this means the original assigned MaNGA IFU is sufficiently large, but requires re-centering. In addition to these already-planned galaxies, two sources of new objects were used. The one galaxy in DR13 with `PAIR_SIM` comes from the Galaxy Zoo Mergers Sample (Holincheck et al. 2016). Finally, to compensate for the bias toward targets that can be observed with a single IFU (close separations or higher redshifts for merging galaxies) and the bias toward red-red mergers in the MaNGA main sample where both galaxies are targeted, additional pairs that each are assigned a separate IFU are added from the targeting catalog with the bitname `PAIR_2IFU`.

- *Massive Nearby Galaxies:* Because the largest MaNGA IFU covers $32''$, more luminous, larger galaxies observed to the same effective radius have poorer spatial resolution. The one `MASSIVE` ancillary target in DR13 is part of a program to obtain a sample of nearby large galaxies with spatial resolution better than 3 kpc and similar to the faintest galaxies in the MaNGA primary sample, at the cost of spatial extent.

- *Milky Way Analogs:* Licquia et al. (2015) defined a sample of Milky Way analogs based on M_*, SFR, absolute magnitudes, and colors. MaNGA is including some of these analogs in the main galaxy catalog, but they are slightly biased or deficient in certain regions of parameter space. Galaxies with the bitname `MWA` are drawn from the Licquia et al. (2015) catalog to provide galaxies in those underrepresented parts of parameter space.

- *Dwarf Galaxies in MaNGA:* The MaNGA main

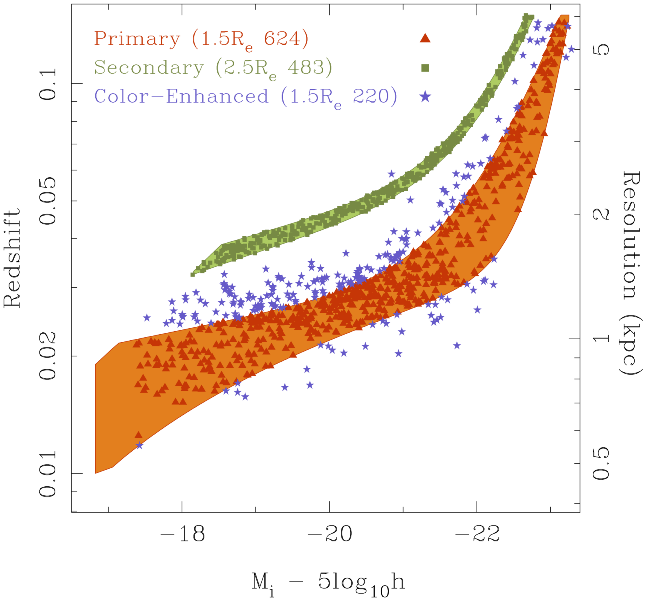

Fig. 4.— Principal selection cuts for the main MaNGA samples, where $h = H_0/100$ km s^{-1}. The colored bands show the selection cuts for the Primary (orange) and Secondary (green) samples illustrating the M$_i$ dependence of the redshift limits. More luminous, and hence typically larger galaxies are selected at higher redshift than less luminous galaxies, ensuring that the angular size (1.5 R_e or 2.5 R_e) distribution is roughly independent of luminosity. The volume sampled also increases as the luminosity increases in such a way as to ensure a constant number density of galaxies at all luminosities. The points show the positions in this plane for the MaNGA galaxies in DR13, for the Primary (red triangles), Secondary (green squares) and Color-Enhanced samples (blue stars), although the Color-Enhanced selection also depends on NUV-$i$color (see text for details). The right hand y-axis gives an indication of the physical size of the mean spatial resolution element of the MaNGA data.

galaxy sample has galaxies with M$_* > 10^9 M_\odot$, but dwarf galaxies are the most numerous galaxies in the Universe. This ancillary program provides 2 dwarf galaxies with MaNGA observations in DR13, the first observations of a larger sample expected by the end of the survey covering a range of environments. These galaxies are indicated by the bitname `DWARF` and are drawn from the Geha et al. (2012) galaxy catalog with stellar masses$< 10^9 M_\odot$.

- *Brightest Cluster Galaxies:* The brightest cluster galaxies (BGCs) targeted here are brighter and in more massive halos than BCGs already in the MaNGA main sample and have the bitname `BCG`. We base our target selection on the updated Yang et al. (2007) cluster catalog, created from the SDSS DR7 NYU VAGC, an update of the DR4 version of Blanton et al. (2005)

- *MaNGA Resolved Stellar Populations:* The ancillary program targets NGC 4163, a nearby dwarf galaxy with existing HST imaging and high-quality

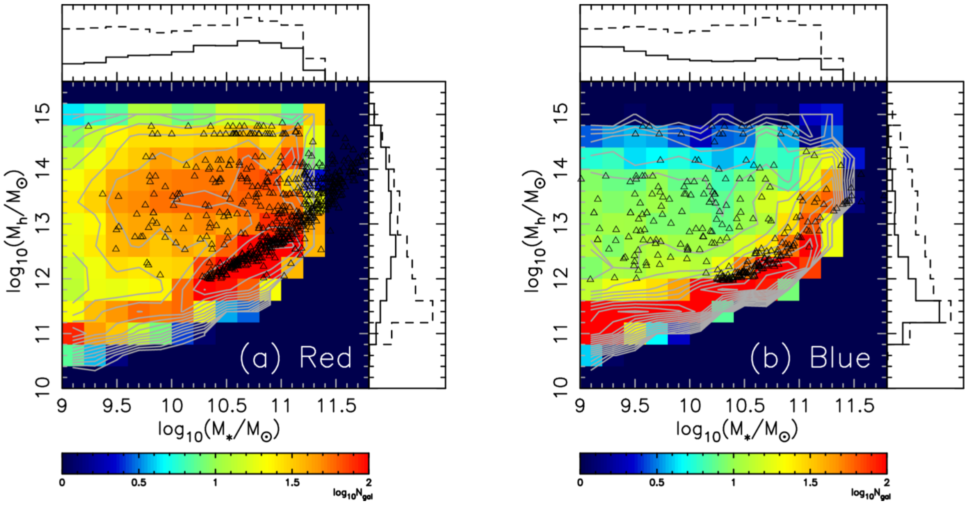

FIG. 5.— MaNGA galaxies in this data release are plotted as black triangles on the plane of stellar mass (M_*, x-axis) versus dark matter halo mass (M_h, y-axis). The two panels show red and blue galaxies separately,which are divided by a single color cut at $g-r=0.7$. Stellar masses are taken from the NASA-Sloan Atlas, and halo masses from SDSS/DR7, using the method of Yang et al. (2007). Plotted in the background are the number of MaNGA galaxies predicted for a 6-year full survey based on mock catalogs informed by the semi-analytic model of Guo et al. (2011) and constructed as in Li et al. (2006), which are the same as Figure 3 of Bundy et al. (2015). Normalized histograms show 1D marginalized M_* distributions (top axes) and M_h distributions (right axes), with dashed lines for the full primary sample and solid lines for the red (left) and blue (right) populations.

color-magnitude diagrams selected from the ACS Nearby Galaxy Survey (Dalcanton et al. 2009). This galaxy is flagged by the bitname `ANGST`.

5.2. *MaNGA Data Products: Individual Fiber Spectra and 3-D Data Cubes*

In DR13, MaNGA is releasing both raw data (in the form of individual CCD frames) and reduced data produced by version 1_5_4 of the MaNGA Data Reduction Pipeline (DRP). Figure 6 illustrates the quality of the spectra from this pipeline. The MaNGA observing strategy is described by Law et al. (2015), and the flux calibration by Yan et al. (2016a). Details of the MaNGA DRP, data products, and data quality are given by Law et al. (2016) (hereafter L16). All MaNGA data are in the form of multi-extension FITS files.

The DRP data products consist of intermediate reduced data (sky-subtracted, flux-calibrated fiber spectra with red and blue data combined for individual exposures of a plate) and final-stage data products (summary row-stacked spectra and data cubes) for each target galaxy. The summary row stacked spectra (RSS files) are two-dimensional arrays provided for each galaxy in which each row corresponds to a single fiber spectrum. For a 127-fiber IFU with 9 exposures, there are thus $127 \times 9 = 1143$ rows in the RSS file. These RSS files have additional extensions giving astrometric information about the wavelength-dependent locations of each fiber on the sky.

The three-dimensional data cubes (axes R.A., Decl., wavelength) are created by combining the individual spectra for a given galaxy together onto a regularized $0.5''$ grid (see L16 for more detail). Both data cubes and RSS files are provided in a version with a log wavelength scale, which is the standard extraction and is relatively smooth in velocity space, and in a version with a linear wavelength scale, created directly from the native pixel solution rather than by resampling the log-scaled spectra resampling. Each MaNGA data cube has associated extensions corresponding to the estimated inverse variance per pixel and a bad-pixel mask containing information about the quality of a given pixel within the cube (depth of coverage, bad values, presence of foreground stars, etc). Additional extensions provide information about the instrumental spectral resolution, individual exposures that went into the composite data cube, reconstructed *griz* broadband images created from the IFU spectra, and estimates of the *griz* reconstructed point spread function.

The objects observed by MaNGA for which data cubes have been produced are summarized in the "drpall" file, a FITS binary table with one entry per object (including both galaxies and spectrophotometric standard stars observed with 7-fiber IFUs to calibrate the MaNGA data). This drpall file lists the name, coordinates, targeting information (e.g., redshift as given by the NASA Sloan Atlas), reduction quality, and other quantities of interest to allow users to identify galaxy targets of interest. We note that MaNGA adopts two naming schemes. The first, termed "mangaid" is an identifier unique to a given astronomical object (e.g., 1-266039). The second, the "plate-ifu" uniquely identifies a given observation by concatenating the plate id with the IFU number (e.g., 7443-12701 identifies the first 127-fiber IFU on plate 7443). Since some galaxies are observed more than once on different plates, a given mangaid can sometimes correspond to more than one plate-ifu.

The mangaid consists of 2 parts separated by a hyphen. The first part is the id of the parent catalog from which a target was selected. The second part is the position within that catalog. For most galaxy targets the catalog id is 1 which refers to the NSA. For a small number of the early targets the catalog id is 12 and refers to an earlier version of the NSA (v1b_0_2). All galaxies from this earlier version of the NSA are also in the final version and so we release photometry etc for those targets from

TABLE 3
Summary of MaNGA Ancillary Programs with Data in DR13

Ancillary Program	Number of Targets [1]	BITNAME	binary digit	value
Luminous AGN	1	AGN_BAT	1	2
	4	AGN_OIII	2	4
Edge-On Star-forming Galaxies	4	EDGE_ON_WINDS	6	64
Close Pairs and Mergers	5	PAIR_ENLARGE	7	128
	10	PAIR_RECENTER	8	256
	1	PAIR_SIM	9	512
	1	PAIR_2IFU	10	1024
Massive Nearby Galaxies	1	MASSIVE	12	4096
Milky Way Analogs	2	MWA	13	8192
Dwarf Galaxies in MaNGA	2	DWARF	14	16384
Brightest Cluster Galaxies	2	BCG	17	131072
MaNGA Resolved Stellar Populations	1	ANGST	18	262144

[1] An individual galaxy can be targeted by more than one ancillary program.

the final version of the NSA (v1_0_1), which is included in the data release. Other catalogs referred to in the first part of the manga-id are for SDSS standard stars.

The full data model for all MaNGA DRP data products can be found online at `http://www.sdss.org/dr13/manga/manga-data/data-model/` and is also given in Appendix B of L16.

5.3. *Retrieving MaNGA Data*

The raw data, reduced data, RSS, and 3-D data cubes for 1351 MaNGA galaxies are provided in DR13. From these data products, maps of line ratios, spectroscopic indices, and kinematics can be made using standard software. Because the first step in using the MaNGA data for science is to retrieve the spectra, we detail here and on the SDSS website[128] how to access the MaNGA spectra.

5.3.1. *Reduced Data Products*

MaNGA DR13 reduced data products are stored on the Science Archive Server at `http://data.sdss.org/sas/dr13/manga/spectro/redux/v1_5_4/`. The top level directory contains the summary drpall FITS table and subdirectories for each plate. Inside each plate directory there are subdirectories for each MJD on which the plate was observed, containing intermediate (exposure level) data products. The 'stack' subdirectory within each plate directory contains the final RSS and cube files for each MaNGA galaxy, sorted according to their plate-ifu identifiers. Note that the ifu identifier in the filenames indicates the size of the IFU; everything in the 127 series (e.g., 12701) is a 127-fiber bundle, etc. The 700 series ifus (e.g., 701) are the twelve spectrophotometric 7-fiber minibundles that target stars on each plate.

These are the ways of getting at the data in DR13:

- Direct html browsing of the SAS at the above link. The file drpall-v1_5_4.fits can be downloaded through the web browser and queried using any program able to read FITS binary tables. Once a set of galaxies of interest has been identified, individual data cubes, summary RSS files, intermediate data products, etc. can be downloaded by browsing through the web directory tree.

- Large downloads of many DRP data products can be automated using rsync access to the SAS. For instance, to download all MaNGA data cubes with a logarithmic wavelength format: `\rsync-aLrvz--include"*/"--include"manga*LOGCUBE.fits.gz"--exclude"*"rsync://data.sdss.org/dr13/manga/spectro/redux/v1_5_4/./`

- The MaNGA drpall file can also be queried online using the SDSS CASJobs system at `http://skyserver.sdss.org/casjobs`. While this can be useful for identifying MaNGA observations of interest, CASJobs does not contain links to the MaNGA data cubes and another method must be used to download the data themselves.

- The SDSS SkyServer Explore tool at `http://skyserver.sdss.org/dr13/en/tools/explore/` will display basic information about MaNGA observations in DR13 that fall within a given cone search on the sky. The relevant explore pages also provide direct links to the FITS data cubes on the SAS.

5.3.2. *Raw Data*

All MaNGA data taken in the first year of SDSS-IV observations are part of Data Release 13, including data from special ancillary plates and co-observing during APOGEE-2 time that are not part of the DRP results. The raw data are stored on the SAS in the directory `http://data.sdss.org/sas/dr13/manga/spectro/data/` in subdirectories based on the MJD when the data were taken. The mangacore directory[129] contains the information needed to figure out the RA and Dec positions of fibers on plates, the dithered MJDs to be combined to make the final spectrum in apocomplete directory, and information on the calibration files. L16 and the `http://www.sdss.org/dr13/manga/manga-data/metadata/` website contain the relevant information about the file formats and the use of the calibration files to get to the fully reduced spectra. Because these files are prepared for internal use, they retain many old features that should be ignored, such as the names assigned to targeting bits, which still retain the names from SDSS-I.

---

[128] `http:www.sdss.org/dr13/manga/manga-data/data-access/`

[129] `http://svn.sdss.org/public/repo/manga/mangacore/tags/v1_2_3/`

5.4. *Notes on using MaNGA data*

There are several important caveats to keep in mind when working with MaNGA data. In this discussion we treat only the MaNGA data cubes. Summary RSS, intermediate, and even raw data products present some statistical advantages to the data cubes, in particular reduced covariance between adjacent data points and greater ease of forward modeling, but are substantially harder to use.

First and foremost, each MaNGA data cube has a FITS header keyword DRP3QUAL indicating the quality of the reduction. 1-2% of the data cubes are flagged as significantly problematic for various reasons, ranging from poor focus to flux calibration problems. Table B13 in L16 lists the bits that can be set with this flag that describe why the end product was deemed unsatisfactory. Galaxies for which the CRITICAL quality bit (=30) is set in DRP3QUAL should be treated with extreme caution. While there may be some spaxels in that data cube that are acceptable, in general the CRITICAL bit indicates widespread problems with the data reduction. Each data cube also has an associated MASK cube describing the quality of individual spaxels in the data cube. This MASK extension can be used to identify areas of no coverage outside the fiber bundle footprint[130], low coverage near the edge of the dithered footprint, problematic areas due to detector artifacts, regions known to contain bright Milky Way foreground stars, etc. A simple summary `DONOTUSE` bit is of particular importance indicating elements that should be masked out for scientific analyses.

Since the MaNGA data cubes adopt a $0.5''$ sampling size (chosen based on Fourier analysis in optimal observing conditions to not truncate the high-k modes of the observational PSF), while individual fibers have a $2''$ diameter footprint, there is significant covariance between adjacent MaNGA spaxels that must be taken into account whenever combining spectra. A simplified method for doing this is discussed in §9.3 of L16. The typical reconstructed point spread function of the MaNGA data cubes has FWHM of $2.5''$.

As discussed by L16, the instrumental line spread function (LSF) in the wavelength direction reported by the various extensions within the MaNGA DR13 data products is underestimated by about $10 \pm 2\%$. Although this makes little difference when determining the astrophysical width of broad spectral lines, it is important to account for when attempting to subtract the instrumental resolution from barely-resolved lines. This issue is not unique to MaNGA; the overestimate is common to all previous SDSS optical spectra. Therefore many reported velocity dispersions in SDSS data are wrong by an amount that becomes significant at velocity dispersions near the instrumental resolution. There are two effects that combine to produce this overestimate. The first is that the impact of the wavelength rectification on the effective spectral resolution was not accounted for when combining spectra from blue and red cameras. The second is that the Gaussian width of the LSF reported by the DRP is strictly the width of a pre-pixellization gaussian, while most end-user analysis routines adopt post-pixellization gaussians instead (i.e., the different between integrating a gaussian profile over the pixel boundaries vs evaluating a gaussian at the pixel midpoint). This will be treated more completely in a future data release; in the meantime a 10% correction to the instrumental LSF quoted by the MaNGA data products appears to be a reasonable correction factor if using post-pixellization analysis routines. However, because this correction factor itself is uncertain, derived astrophysical line-widths substantially below the instrumental resolution should be viewed to have unreliable accuracy at this time. A full discussion of issues to consider is available at `http://www.sdss.org/dr13/manga/manga-caveats/`.

5.5. *Highlights of MaNGA Science with DR13 Data*

The MaNGA survey has produced a number of scientific results based on early data, indicating the breadth of research possible with the MaNGA data. Here we briefly summarize the results of papers completed within the SDSS-IV collaboration using MaNGA data on spatially resolved gas physics, stellar population properties, and stellar and gas kinematics. These papers serve as a guide to prospective users of SDSS-IV data in these specific science areas. The papers also provide citations to the extensive literature on each topic, to which we refer the interested reader for additional context.

5.5.1. *Gas physics*

The spatially resolved emission-line measurements have been used to understand the physical conditions of the ionized gas in galaxies. Cheung et al. (2016) identified AGN winds as a surprisingly common occurrence in normal, quiescent galaxies, suggesting these winds as potentially critical in suppressing star formation. These winds may help address the question of how star formation remains suppressed in early-type galaxies. Cheung et al. (2016) report bisymmetric emission features co-aligned with strong ionized-gas velocity gradients in a galaxy from which they infer the presence of centrally driven winds in typical quiescent galaxies that host low-luminosity active nuclei. These galaxies account for as much as ten per cent of the quiescent population with masses around $2 \times 10^{10}\ M_\odot$. They calculate that the energy input from the galaxies' low-level active supermassive black hole is capable of driving the observed wind, which contains sufficient mechanical energy to heat ambient, cooler gas (also detected) and thereby suppress star formation.

The broader nature of ionized gas in early-types has also been the subject of papers by Belfiore et al. (2016) and Belfiore et al. (in preparation) following up on the analysis of a small sample observed with the MaNGA prototype instrument in Belfiore et al. (2015). By using spatially resolved maps of nebular diagnostics *and* stellar population ages, this work has added substantial support to the notion that evolved stellar populations provide the ionization source for a galaxy class that arguably should be renamed from LINER (Low Ionization Nuclear Emission Region) galaxies to LIER galaxies. LIERs, it turns out, are ubiquitous in both quiescent galaxies and in the central regions of galaxies where star formation takes place at larger radii. The study of Belfiore et al. (2016)

---

[130] The fiber footprint is a hexagon, but the standard FITS image data structure is based around rectangular arrays. There must therefore be blank areas around the live IFU footprint in order to inscribe the hexagon inside a bounding rectangle.

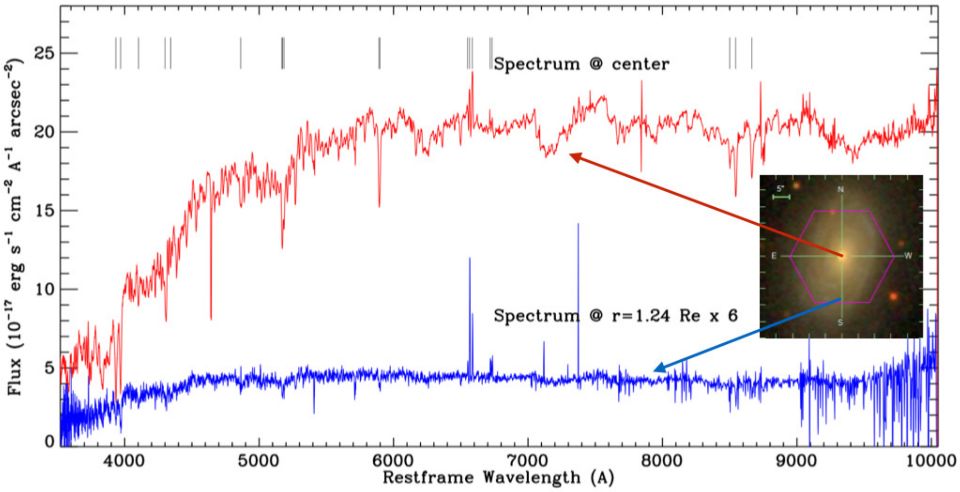

Fig. 6.— Example spectra from a typical MaNGA data cube, adapted from Yan et al. (2016b). The inset shows the SDSS color image with the hexagonal IFU footprint overlayed. The top spectrum is from the central spaxel; the bottom spectrum from a spaxel 1.2 R_e from the center and is multiplied by a factor of 6 for easier comparison with the central spectrum. The differences in the stellar and gas components between the two regions can clearly be seen, as well as the large number of diagnostic features to understand the star formation history and the physical conditions of the gas.

and Belfiore et al. (in prep) have put the occurrence of the LIER phenomenon into a physically relevant framework that can be directly tied to the diversity of the galaxy population as a whole. Specifically, they identify two classes of galaxies as extended LIER (eLIER) and central LIER (cLIER), respectively, and study their kinematics and stellar population properties. cLIERs turn out to be mostly late type galaxies located around the green valley, while eLIERs are morphologically early types and are indistinguishable from passive galaxies devoid of line emission in terms of their stellar populations, morphology and central stellar velocity dispersion.

The widespread ionization state of LIER gas might originally manifest as the Diffuse Intergalactic Gas (DIG) which is intermixed with star-forming regions. Zhang et al. (2016) studied galactic DIG emission and demonstrate how DIG in star-forming galaxies impacts the measurements of emission line ratios at the spatial resolution of MaNGA, hence the interpretation of diagnostic diagrams and the gas-phase metallicity measurements. They quantify for the MaNGA data how the contamination by DIG moves HII regions towards composite of LIER-like regions. DIG significantly biases measurements of gas metallicity and metallicity gradients because at different surface brightness, line ratios and line ratio gradients can differ systematically.

A careful treatment of gas-phase metallicities inferred from spectral maps of galaxies has suggested a key role for the dependence of metallicity on local stellar mass surface density. Barrera-Ballesteros et al. (2016, submitted) present the stellar surface mass density vs gas metallicity relation for more than 500,000 spatially-resolved star-forming regions from a sample of 653 disk galaxies. These galaxies span a larger range in mass than in previous samples where the correlations were first discovered. They confirm a tight relation between these local properties, with higher metallicities as the surface density increases. They find that even over this larger mass range this local relationship can simultaneously reproduce two well-known properties of disk galaxies: their global mass-metallicity relationship and their radial metallicity gradients. Their results support the idea that in the present-day universe local properties play a key role in determining the gas-phase metallicity in typical disk galaxies.

However, Cheung et al. (2016b, submitted) have found a galaxy in the middle of a gas accretion event, providing a detailed look at what appears to be a relatively rare occurrence in the nearby Universe of this mode of galaxy growth. They present serendipitous observations of a large, asymmetric Hα complex that extends $\sim 8''$ (~ 6.3 kpc) beyond the effective radius of a dusty, starbursting galaxy. This Hα extension is approximately three times the effective radius of the host galaxy and displays a tail-like morphology. This is suggestive of an inflow, which is consistent with its relatively lower gas-phase metallicities and its irregular gaseous kinematics.

5.5.2. *Stellar populations*

Spatially resolved stellar population properties and stellar growth histories have been analyzed, following the analysis of a small sample observed with the MaNGA prototype instrument by Wilkinson et al. (2015) and Li et al. (2015). MaNGA has explored the role of environment in shaping the radial distribution of stellar ages and metallicities, with particular attention given to the potential measurement systematics. Using different spectral fitting techniques and complementary environmental metrics, both Goddard et al. (2016b, submitted) and Zheng et al. (2016, submitted) conclude that any environmental signal in the average shape of gradients is weak at best, with no obvious trends emerging in the initial MaNGA data.

Goddard et al (2016a, submitted) studied the internal gradients of the stellar population age and metallicity within 1.5 R_e obtained from full spectral fitting and confirm several key results of previous surveys. Age gradients tend to be shallow for both early-type *and* late-type galaxies. As well known from previous studies, metallicity gradients are often complex (and *not* well-modeled by linear or log-linear functions of radius), varying in detail from galaxy to galaxy on small radial scales. On average, however, over radial scales of order 1 $R_{\rm e}$, MaNGA data provide the strongest statistical constraints to date that metallicity gradients are negative in both early and late-type galaxies, and are significantly steeper in disks. These results continue to indicate that the radial dependence of chemical enrichment processes are far more pronounced in disks than they are in spheroids, and indeed the relatively flat gradients in early-type galaxies are inconsistent with monolithic collapse. For both early and late-type galaxies, more massive galaxies have steeper negative metallicity and age gradients. Since early-type galaxies tend to be more luminous, the overall steeper age and metallicity gradients in late-type galaxies reflect the fact that the trends in these gradients with galaxy mass are more pronounced for late-type galaxies. Goddard et al (2016a, submitted) take advantage of the unique MaNGA sample size and mass range to characterize this correlation between metallicity and age gradients and galaxy mass, which explains the scatter in gradients values seen in previous studies.

Ibarra-Medel et al. (2016, submitted) meanwhile infer spatially-resolved stellar mass assembly histories for the MaNGA galaxies, extending previously known relations between galaxy type and assembly history to a larger mass range. Their findings are consistent with blue/star-forming/late-type galaxies assembling, on average, from inside to out. Red/quiescent/early-type galaxies present a more uniform spatial mass assembly, or at least one that has been dynamically well mixed since star-formation ceased, consistent with the flatter gradients seen, e.g., by Goddard et al (2016a, submitted). In general, low-mass galaxies show evidence of more irregular global and spatial assembly histories than massive galaxies.

In a developing effort to model stellar population gradients, Johnston et al. (2016, submitted) demonstrate a new technique using MaNGA data that seeks to decompose the underlying population into contributions from different physical sub-components. They explore how the disk and bulge components in galaxies reached their current states with a new approach to fit the two-dimensional light profiles of galaxies as a function of wavelength and to isolate the spectral properties of these galaxies' disks and bulges. The MaNGA data have a spatial sampling of 0.5 $''$ per pixel, and successful decompositions were carried out with galaxies observed with the 61- to 127-fiber IFUs with fields of view of 22$''$ to 32$''$ in diameter respectively.

Rembold et al. (2016, submitted) have identified a "control sample" to the MaNGA luminous AGN host galaxies, matched on mass, distance, morphology, and inclination. Their conclusions based on SDSS-III spectra of the central region can be tested with evaluation of the stellar populations throughout the galaxies with MaNGA data.

5.5.3. *Gas and stellar kinematics*

Several studies are investigating the kinematics of both stars and gas across the galaxy population. Li et al. (2016b, submitted) perform dynamical modeling on a more extensive and diverse sample of elliptical and spiral galaxies than had previously been done. By comparing the stellar mass-to-light ratios estimated from stellar population synthesis and from dynamics, they find a similar systematic variation of the initial mass function (IMF) to previous investigations. Early-type galaxies (elliptical and lenticular) with lower stellar mass-to-light ratios or velocity dispersions within one effective radius are consistent with a Chabrier-like IMF while galaxies with higher stellar mass-to-light ratios or velocity dispersions are consistent with a more bottom heavy IMF such as the Salpeter IMF.

Two studies have taken advantage of the large MaNGA sample in DR13 to quantify the frequency and attributes of galaxies with strong disparities between gas and stellar kinematics. Chen et al. (2016, submitted) find that an appreciable fraction of galaxies have counter-rotating gas and stars. Counter-rotation is found in about 2% of all blue galaxies. The central regions of blue counter-rotators show younger stellar populations and more intense star formation than in their outer parts. Jin et al (2016, submitted) have further studied the properties of 66 galaxies with kinematically misaligned gas and stars. They find that the star-forming misaligned galaxies have positive gradients in D_n4000 and higher gas-phase metallicity, while the green valley/quiescent ones have negative D_n4000 gradients and lower gas-phase metallicity on average. Despite this distinction, there is evidence that all types of kinematically-misaligned galaxies tend to be in more isolated environments. They propose that misaligned star forming galaxies originate from gas-rich progenitors accreting external kinematic decoupled gas, while the misaligned green valley/quiescent galaxies might be formed from accreting kinematic decoupled gas from dwarf satellites.

Finally, Penny et al. (2016, in press) examine the kinematics of a sample of 39 quenched low-mass galaxies. The majority (87%) of these quenched low mass galaxies exhibit coherent rotation in their stellar kinematics, and a number host distinct disks or spiral features. Just five (13%) are found to have rotation speeds $v_{\rm circ} < 15$ km s^{-1} at 1 R_e, and are dominated by pressure support at all radii. Two of the quenched low mass galaxies (5%) host kinematically distinct cores, with the stellar population at their centers counter-rotating with respect to the rest of the galaxy. The results support a picture in which the majority of quenched low mass (dE) galaxies have a disk origin.

6. SEQUELS: EBOSS, TDSS, AND SPIDERS DATA

DR13 includes the data from 126 plates observed under the SEQUELS program. This program was started in SDSS-III as an ancillary program to take advantage of some of the dark time released when BOSS was completed early. The SEQUELS targets were quite different from BOSS targets because the program was designed to finalize the eBOSS target selection algorithms. The primary targets were defined by two different SDSS-WISE selection algorithms to determine the eBOSS LRG program (Prakash et al. 2016) and several optical-IR and variability selections to determine the eBOSS quasar program (Myers et al. 2015). Likewise, objects selected from a combination of X-ray and optical imaging were used to determine the final SPIDERS cluster (Clerc et al. 2016, submitted) and AGN (Dwelly et al., in preparation) programs while variability in PanSTARRS imaging was used to determine the final TDSS program (Morganson et al. 2015; Ruan et al. 2016).

66 SEQUELS plates were completed in the final year of SDSS-III. The remaining 60 plates required to fill out the 400 square degree footprint were completed in the first year of SDSS-IV. As mentioned above, these data served a crucial role for verification of the eBOSS, TDSS and SPIDERS target samples. SEQUELS and eBOSS LRG spectra were used to optimize the performance of a new redshift classification scheme that now reliably classifies more than 90% of eBOSS LRG spectra (Hutchinson et al. 2016, submitted), thus meeting the ambitious goal set forth at the beginning of the program (Dawson et al. 2016). The sample also seeds the eBOSS footprint to be used for clustering studies. The first clustering measurements from SEQUELS and eBOSS LRGs were just released (Zhai et al. 2016) and first results from quasar clustering are expected in the near future. All SEQUELS targets are tracked by the `EBOSS_TARGET0` bitmask. The appendix of the DR12 paper (Alam et al. 2015) provides the motivation and description of each target selection algorithm captured by that bitmask.

6.1. *eBOSS in SEQUELS*

117 plates from SEQUELS used a slightly broader selection for LRG, clustering quasars ($0.9 < z < 2.2$), and Lyman-α forest quasars to ensure that the final eBOSS selection would be included in each of these classes. Because the eBOSS sample is included in this region, the SEQUELS spectroscopy obtained in SDSS-III and SDSS-IV will be used directly in any LRG or quasar clustering studies. Nine plates from SEQUELS, all released in DR12, included targets derived from an early test of the ELG selection algorithm (Alam et al. 2015). These tests of ELG selection algorithms were part of a larger series of tests performed during SDSS-III and SDSS-IV (Comparat et al. 2015; Raichoor et al. 2016; Delubac et al. in preparation). The spectra from these tests were also used in one of the first science results from eBOSS, a study of galactic-scale outflows traced by UV emission (Zhu et al. 2015). The selection algorithm used in these fields is quite different from what will be used in eBOSS and these targets will not contribute to the final clustering sample. For this reason, we summarize the findings of the LRG and quasar spectra below but reserve discussion of the ELG spectra for future work.

DR13 does contain value-added catalogs relevant to ELG sample. Raichoor et al. (2016) describe the Fischer discriminant used to select ELG targets using photometry from SDSS, WISE, and SCUSS (Zou et al. 2016) for the main ELG sample. Delubac et al. (in preparation) produce the catalogs used for ELG targeting with SDSS+WISE or SDSS+WISE+SCUSS data. Finally, Zhu et al. (2015) generated composite, continuum-normalized, spectra of emission-line galaxies in the rest-UV from ELGs observed by BOSS in various programs. Table 2 lists the location of these files on the SAS.

6.1.1. *Luminous Red Galaxies from WISE colors*

The increase in redshift complicates selection both by shifting the 4000 Å break into the i-band filter and by requiring fainter targets than those observed in BOSS. WISE 3.4 μm photometry (W1 band) was introduced to enable selection of this higher redshift sample. As part of the SEQUELS program, two overlapping selections for LRGs at higher redshifts ($0.6 < z < 1.0$, vs $0.4 < z < 0.7$ for CMASS) were employed, allowing tests of potential strategies for eBOSS. Color cuts that combine optical and infrared photometry were employed, enabling the targeting of LRGs at these redshifts while maintaining a high purity. This selection technique takes advantage of the strong peak at a rest frame wavelength of 1.6 microns that is present in the spectrum of most galaxies. This peak enters W1 as the redshift gets closer to 1, yielding large differences between the optical/IR colors of $z > 0.6$ galaxies and stars.

SEQUELS selected a total of $\sim 70,000$ LRGs over an area of ~ 700 deg^2 with $120.0 < \mathrm{RA} < 210.0$ and $45.0 < \mathrm{DEC} < 60.0$. These LRGs were selected by algorithms utilizing two different optical-IR color spaces, utilizing either SDSS r, i, z, and W1, or only i, z and W1; the selection efficiency and redshift success for each algorithm could then be compared. The parameters of the selection algorithms were tuned such that each yielded a target density of ~ 60 deg^{-2}; the two selections overlap significantly, yielding a net density of 72 targets deg^{-2}. Figure 10 of Prakash et al. (2016) presents the resulting redshift distributions from each selection. The $r/i/z/$WISE selection has been chosen for eBOSS due to greater efficiency at selecting high-redshift LRGs. More details on the SEQUELS LRG sample selection can be found in Prakash et al. (2016).

6.1.2. *Quasars targeted with Optical+WISE photometry and photometric variability*

SEQUELS observations helped define a uniform quasar sample for eBOSS clustering studies based on $ugriz$ and WISE photometry. The "Extreme Deconvolution" (XDQSO; Bovy et al. 2011a,b) selection is used to identify likely quasars at redshifts $z > 0.9$ according to the relative density of stars and quasars as a function of color, magnitude, and photometric uncertainty. The selection alone results in a highly complete sample of quasars to be used for clustering studies, but with contamination from stars that is too large to fit into the eBOSS fiber budget. The XDQSO selection is supplemented by morphology cuts to remove low redshift AGN and optical-IR colors to remove stellar objects with blackbody spectra. Variability data from the Palomar Transient Factory (PTF; Law et al. 2009) are used to supplement the selection of Lyman-α forest quasars, producing tracers with a density of 3.2 deg^{-2} where sufficient PTF imaging data are available. In addition to cosmological measurements, the quasar sample can be used to study quasar astrophysics and galaxy evolution through studies of the quasar luminosity function, composite spectra, and multi-wavelength spectral energy distributions spanning the radio to the X-ray. Myers et al. (2015) found that ~ 96 of all quasar targets with $r < 22$ will be confidently classified. Section 5 of Myers et al. (2015) provides information on the properties of quasars observed with SEQUELS, including the numbers observed in the redshift ranges $0.9 < z < 2.1$ and $z > 2.1$.

DR13 includes value-added catalogs with the variability measurements (see Palanque-Delabrouille et al. 2011) using either PTF data (Myers et al. 2015) or Stripe 82 data (Palanque-Delabrouille et al. 2016) that are used for selecting quasars in eBOSS based on variability. The locations of the FITS tables are given in Table 2.

6.1.3. *Redmonster and Improved Redshifts for LRGs*

The DR13 redshifts for all SEQUELS targets are determined in the usual fashion, with best-fitting combinations of PCA eigenspectra. Hutchinson et al. (2016, submitted) describe a new pipeline, `redmonster` that uses a suite of discrete theoretical galaxy spectra as a basis to determine the most likely redshift through a minimum χ^2, rather than linear combinations of templates used in Bolton et al. (2012). This pipeline achieves a 90.5% automated redshift and spectral classification success rate for the LRG target class, a significant improvement over the performance of the previous pipeline. A value-added catalog using the new `redmonster` algorithms for the LRG sample is included in DR13. All spectra identified by `EBOSS_TARGET0` bit 1 or 2 were classified by redmonster. The file is named `redmonsterAll-v5_9_0.fits` and is found on the SAS as described in Table 2.

6.2. *SPIDERS in SEQUELS*

The main goal of the SPIDERS survey is to characterize a subset of X-ray sources identified by eROSITA using optical spectra from the BOSS spectrograph. The extended sources will mostly be galaxy clusters, which can be used for cosmology. The point sources will mainly be AGN, which can be used to study the evolution of black holes across cosmic time. For the first phase of SDSS-IV, when eROSITA data are not yet available, SPIDERS will be targeting based on ROSAT and XMM data. The target catalogs for galaxy clusters and AGN for SPIDERS from these two satellites have been included in DR13 as value-added catalogs. The SPIDERS AGN target catalogs (Dwelly et al., in preparation) contain 9,028 candidate targets from RASS and 819 from XMMSL (**XMM**-Newton **Sl**ew survey catalog; Saxton et al. 2008). They enclose information on the X-ray sources, including flux measurements, and a quantitative measure of the reliability of the association to optical and AllWISE data. The SPIDERS Galaxy Cluster target list (Clerc et al, submitted) contains 94,883 and 3,839 objects for RASS and XMM respectively.

In SEQUELS, SPIDERS used similar targeting catalogs, also available as value-added products, to test targeting strategies and provide initial results. The selection criteria are somewhat different than the final SPIDERS algorithms. Full details are available in Clerc et al. (2016, submitted) and Dwelly et al. (in preparation). We summarize the SEQUELS SPIDERS data available in DR13 below.

6.2.1. *Optical spectra of Galaxies in X-ray Identified Clusters*

The cluster pilot study (Clerc et al. 2016, submitted) takes advantage of the CODEX (**Co**nstrain **D**ark **E**nergy with **X**-ray clusters; Finoguenov et al., in preparation) candidate cluster list, which is based on currently available RASS data. As part of DR13, we provide the catalog of X-ray detected galaxy clusters spectroscopically confirmed using SEQUELS-DR12 SPIDERS spectroscopic data. Galaxy clusters were identified through the emission of their hot baryonic component as extended X-ray sources in RASS. The optical counterparts were found by optimally searching photometric data for the existence of a red-sequence formed by their member galaxies. Spectroscopic redshifts obtained by SPIDERS provide definitive confirmation of the clustered nature of these objects and their redshift (up to $z \sim 0.6$). We assigned cluster membership combining an algorithm and visual validation of individual objects. The gas properties derived from X-ray observations (luminosity, temperature, R_{200}[131]) are derived using precise cluster redshifts ($\Delta_z \sim 0.001$). We compute galaxy cluster velocity dispersions using several methods adapted to the low number of spectroscopic members per system (of the order 15-40) and we show that their values correlate with cluster X-ray luminosities, within expectations. Figure 7 shows the distribution of clusters with SEQUELS redshifts and membership in the redshift-X-ray luminosity plane.

6.2.2. *Optical spectra of X-ray-identified AGN*

The addition of X-ray-identified AGN to the suite of AGN with well-sampled redshifts helps complete the inventory of AGN and trace black hole growth throughout cosmic history. SDSS has been observing optically-identified AGN since its inception under the main large-scale structure surveys, special targeting programs, and as "mistakes" in other targeting classes. In addition, there were several BOSS ancillary programs focused on X-ray follow-up, including a highly complete program on the XMM-XXL north field (Menzel et al. 2016). The SPIDERS SEQUELS program has added spectra of 274 ROSAT AGN to the SDSS sample, identified on the basis of their SDSS colors only. The DR12 paper (Alam et al. 2015) and Dwelly et al. (in preparation) provide details on the targeting of these AGN.

6.3. *TDSS in SEQUELS*

Nearly 18,000 targets selected or co-selected by TDSS have been observed among the 126 SEQUELS spectroscopic plates. The targeting strategy for TDSS in SEQUELS was very similar to that ultimately chosen for the bulk of SDSS-IV (Morganson et al. 2015). Ruan et al. (2016) present TDSS spectroscopic results from the 66 initial DR12 SEQUELS plates, along with a description of the small differences in targeting within SEQUELS. Figure 8 depicts results for the initial TDSS

---

[131] R_{200} is defined as usual as the radius where the mean overdensity is equal to 200× the critical density.

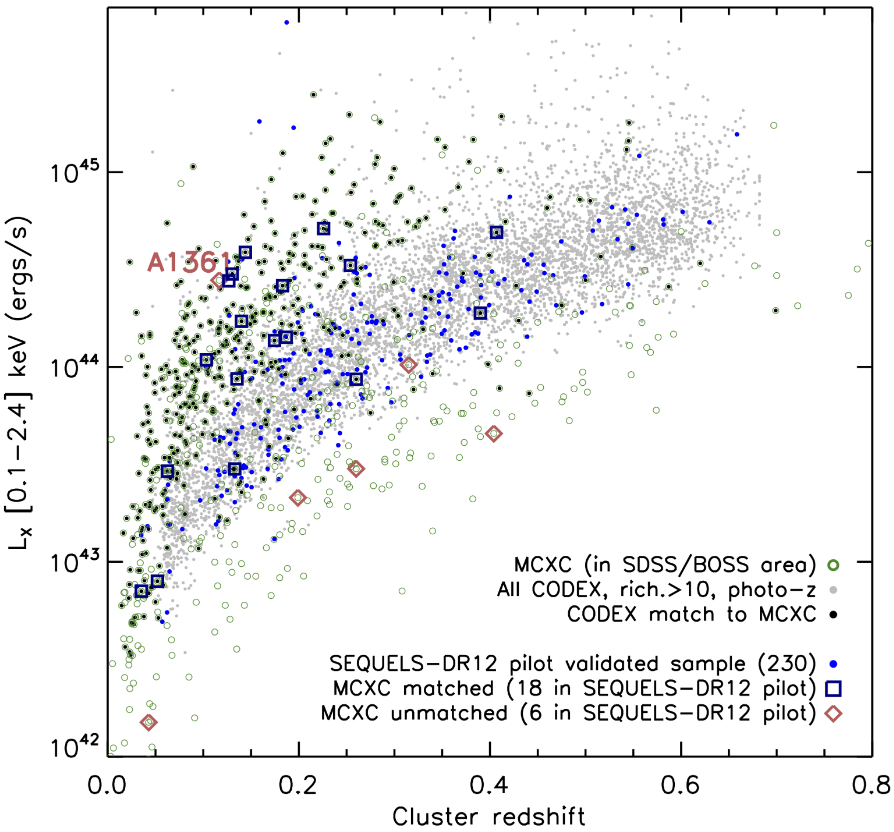

Fig. 7.— Distribution in the X-ray luminosity-redshift plane of galaxy clusters, adapted from Clerc et al. (2016, submitted). The gray dots mark the location of all candidate CODEX clusters using their photometric redshift. They form the main pool of cluster targets in SPIDERS. The CODEX candidate clusters that have already been spectrocopically confirmed and included in the MCXC meta-catalog (Piffaretti et al. 2011) are indicated by open symbols. The confirmed clusters lie mainly at higher X-ray luminosities. The 230 confirmed clusters in the SPIDERS DR13 value-added catalog (blue dots) extend the redshift range of known clusters in the SDSS area to $z \sim 0.6$ in a systematic way. Among these 230, only 18 match clusters from the MCXC meta-catalog. The new clusters in general lie at lower X-ray luminosities and therefore probe lower X-ray masses than previous ROSAT-based analyses. The 6 clusters indicated by red diamonds are MCXC clusters in the SEQUELS-DR12 footprint not present in SPIDERS (note that ABELL 1361 is within a masked area of the CODEX survey, so it is not matched).

SEQUELS sub-sample. The classification of spectra was initially done using the BOSS pipeline (Bolton et al. 2012), but the spectra were also visually inspected. Overall, the pipeline performance is outstanding, with the highest-level spectral classification (e.g., star vs. galaxy vs. quasar) in agreement with our visual inspection for about 97% of the TDSS spectra and with only 2% of the pipeline redshifts for quasars requiring significant adjustment.

About 90% of the TDSS spectroscopic fibers are aimed at initial classification spectra for variables chosen without primary bias based on color or specific lightcurve character. Their variability is determined from within PS1 multi-epoch imaging (Kaiser et al. 2010), or via longer-term photometric variability between SDSS and PS1 imaging surveys (Morganson et al. 2015). The initial SEQUELS results reveal comparable numbers of stars and quasars among these photometric variables. A summary for TDSS quasars is that the PS1/SDSS variability criteria mitigate some of the (well-known) redshift biases of color-selection yielding a smooth and broad quasar redshift distribution, and that TDSS selects relatively redder quasars (e.g., than the eBOSS core quasar sample) as well as a higher fraction of some peculiar AGN (such as BALQSOs, and BL Lacs); and among variable stars, TDSS selects significant numbers of active late-type stars, stellar pulsators such as RR Lyrae, and eclipsing and composite binaries, along with smaller subsets of white dwarfs, cataclysmic variables, and carbon stars (see Ruan et al. 2016).

The other ∼10% of the TDSS targets are objects already having one or more earlier epochs of SDSS I-III spectroscopy, and for which TDSS is taking a second (or sometimes 3rd or 4th etc.) epoch to reveal anticipated spectroscopic variability. These "Few Epoch Spectroscopy" (or FES) targets include various subsets of quasars and stars (Morganson et al. 2015). Recent example science papers representative of this FES category of TDSS, include work on acceleration of broad absorption lines in BALQSOs (e.g., Grier et al. 2016), and recent discoveries adding to the rare class of "changing look quasars" (e.g., Runnoe et al. 2016).

6.4. *Retrieving SEQUELS data*

All SDSS data releases are cumulative and therefore the SEQUELS data, whether taken in SDSS-III or SDSS-

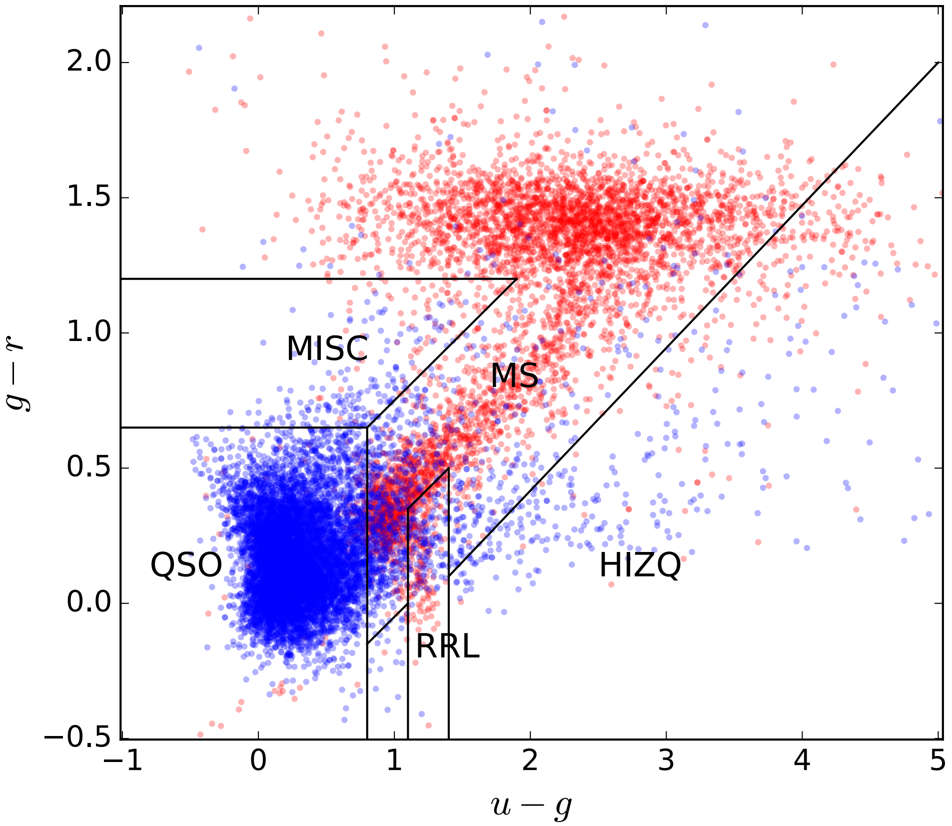

Fig. 8.— A representation of the TDSS spectroscopic characterization of imaging variables selected (from PanSTARRS 1 and SDSS imaging) without any primary bias based on color or specific lightcurve character. Nearly 16,000 TDSS photometric variables in the region of the sky covered by the 66 initial SEQUELS plates are plotted here in a traditional color-color diagram. Their classifications are based on spectra taken in SDSS-I-III, including SEQUELS data. Regions in color space traditionally considered as occupied by quasars, main-sequence stars, RR Lyrae, high-redshift quasars, and other miscellaneous subclasses are overlayed (see Sesar et al. 2007, but here using specific boundaries detailed in Morganson et al. 2015). The blue symbols depict TDSS photometric variables whose SDSS spectra verify them as quasars, while the red symbols depict TDSS variables whose SDSS spectra verify them as stars. A few hundred objects that were identified as galaxies or which could not be identified are not included in this plot. The wide distribution, as well as the overlap (in some regimes relatively densely), of both stars and quasars symbols verify that TDSS variability selection finds not only traditional quasars, but also those within color regimes commonly attributed to stars (and with analogous results for the spectroscopically confirmed variable stars).

IV, have been reduced with the latest pipelines and included with all previous SDSS optical spectra data in this data release. SEQUELS targets can be identified because the `EBOSS_TARGET0` bit will be set. The summary spAll-v5_9_0.fits datafile, which includes classification information from the pipeline, is at `https://data.sdss.org/sas/dr13/eboss/spectro/redux/v5_9_0/` on the SAS or in the specObjAll table on the CAS.

7. APOGEE-2: IMPROVED SPECTRAL EXTRACTION AND SPECTROSCOPIC PARAMETERS FOR APOGEE-1 DATA

The data released in DR13 are based on the same raw data as in DR12, and the pipelines for reduction and analysis remain similar to those used in DR13. First, the data reduction pipeline (Nidever et al. 2015) reduced the 3-D raw data cubes into well-sampled, combined, sky-subtracted, telluric-corrected and wavelength-calibrated 1-D spectra. The stellar parameters and abundances were derived using ASPCAP (**A**POGEE **S**tellar **P**arameters and **C**hemical **A**bundances **P**ipeline; García Pérez et al. 2016) by finding the χ^2 minimum when comparing the normalized observed spectra against a grid of synthetic spectra. However, the processing and analysis have been improved in several ways:

- The linelist used for determining stellar parameters and abundances has been revised.

- Abundances are derived for several more species (C I, P, Ti II, Co, Cu, Ge, Rb) than in DR12.

- Results are now available for stars with $T_{\rm eff} <$ 3500 using a newly employed MARCS model atmosphere grid.

- Separate synthetic spectral grids are used for dwarfs and giants; results for dwarfs include rotation and different isotope ratios are used for dwarfs and giants.

- An initial, approximate, attempt has been made to account for variable LSF as a function of fiber number.

- The correction for telluric absorption has been improved, primarily from a better LSF characterization, leading to better recovery of the stellar spectra.

- The relation adopted from microturbulence has been refined, and a relation for macroturbulence has been incorporated.

More details are provided in Holtzman et al (2016, in preparation; H16). Overall, these changes have improved and enhanced the APOGEE stellar parameters and abundances, but users need to continue to be aware of potential issues and data flagging, as discussed on the SDSS web site and H16. In particular, parameters and abundances for low metallicity stars and for cool stars are more uncertain.

Subsequent to the freezing of the DR13 release, several issues were discovered with the "calibrated" effective temperatures and surface gravities that are released with DR13. Based on good agreement of the spectroscopic effective temperature with photometric effective temperatures for the bulk of the sample that is near solar-metallicity, no calibration was applied to the DR13 spectroscopic effective temperatures. It now appears, however, that these are systematically offset from photometric temperatures for stars of lower metallicity by as much as 200-300 K for stars at [Fe/H][132] ~ -2. For surface gravities, a calibration was derived based on asteroseismic surface gravities. While this calibration is good for most of the sample, it now appears that it does not yield accurate surface gravities for metal-poor stars; the calibrated surface gravities for stars with [M/H][133]< -1.5 are systematically too low, by as much as ~ 0.5 dex. H16 and the SDSS web site discuss both of these issues, and suggest post-release calibrations.

7.1. *Improvements in Linelist and Data Analysis*

Several improvements were made with regard to the APOGEE LSF. The characterization of the LSF was improved in one of the detectors, and an initial attempt was made at accommodating the LSF variability in the parameter and abundance pipeline by constructing spectral libraries for 4 different LSFs and using the most appropriate one for the analysis of each star.

The linelist adopted for DR13, linelist.20150714, is an updated version of the one used for DR12 results (Shetrone et al. 2015) and is available at `http://data.sdss.org/sas/dr13/apogee/spectro/redux/speclib/linelists/`. Shetrone et al. (2015) noted a number of concerns with the DR12 linelist, which have been corrected in the new version (H16). As in DR12, the molecular line list is a compilation of literature sources including transitions of CO, OH, CN, C2, H2, and SiH. The CN line list has been updated from the DR12 version using a compilation from C. Sneden (private communication). All molecular data are adopted without change, with the exception of a few obvious typographical corrections. The atomic line list was compiled using a number of literature sources for the lower excitation state of the transition and the transition probability, which is usually characterized as the "gf" or "log gf" value. Literature sources include theoretical, astrophysical, and laboratory gf values. A few new lines were added from NIST5[134] and other literature publication since the DR12 line list was created, including hyperfine splitting components for Al and Co. We still rely heavily on "astrophysical" gf values for atomic lines, where the transition probabilities of individual lines are determined using the spectrum of a star with known parameters and abundances, to construct linelists in the H-band (Meléndez & Barbuy 1999; Ryde & Schultheis 2015). For our linelist, we use the center-of-disk spectrum of the Sun (Livingston & Wallace 1991) and the full disk spectrum of the nearby, well-studied, red giant Arcturus (Hinkle et al. 1995). To calculate the astrophysical gf values, we used Turbospectrum (Alvarez & Plez 1998; Plez 2012) to generate synthetic spectra of the center-of-disk for the Sun and the integrated disk for Arcturus with varying oscillator strengths and damping values to fit the solar and Arcturus spectra. In DR12, a different stellar atmosphere code was used for the gf determination and the synthetic grid creation and synthetic integrated disk spectra were used for the both the Sun and Arcturus. Although the change in gf values from these changes is small (Shetrone et al. 2015), the DR13 linelist is more self-consistently generated than previous versions. In DR12, we derived final astrophysical gf values by weighting the solar astrophysical gfs at twice those of Arcturus. The astrophysical gf solutions in DR13 are weighted according to line depth in Arcturus and in the Sun, to give more weight to where the relatively weak lines in the H-band produce the best signal, which usually gives more weight to the Arcturus solution. For lines with laboratory oscillator strengths, the astrophysical log(gf) values were not allowed to vary beyond twice the error quoted by the source.

7.2. *Additional Elements*

In DR13, APOGEE provides abundances for elements P, Cr, Co, Cu, Ge, and Rb for the first time. The abundances of C, N, O, Na, Mg, Al, Si, S, Ca, Sc, Ti, V, Mn, Fe, and Ni were re-derived. We added two new species: C I and Ti II, which provide valuable checks on the abundances derived from CH and Ti I lines (H16). The technique for calculating abundances of individual elements is described in Holtzman et al. (2015). As for DR12 and as discussed in Holtzman et al. (2015), we correct abundance ratios [X/Fe][135], except for [C/Fe] and [N/Fe], so there is no trend with temperature among the members of a single star cluster. In Figure 9, we show the mean value and the rms scatter for the abundances for member stars in four clusters with a range of metallicity. Both the mean values and the rms illustrate key points about the APOGEE DR13 abundances.

- The elements cover a wide range in nucleosynthesis sites and atomic number. APOGEE is measuring the abundances of α-elements, odd-Z elements, iron-peak elements, and neutron-capture elements, as well as the mass, mixing and AGB-contribution diagnostics C and N.
- The high [X/Fe] for the α elements in the metal-poor ([Fe/H]< -0.7) globular clusters is present as

---

[132] $[X/H]=(\log_{10}(N_X/N_H))_* - (\log_{10}(N_X/N_H))_\odot$. $[X/Fe]=[X/H]_* - [Fe/H]_*$.

[133] [M/H] is closely related to [Fe/H]. See Mészáros et al. (2013) for more details.

[134] `http://www.nist.gov/pml/data/asd.cfm`

[135]

expected (Wallerstein 1962). The increased scatter in O, Mg, and Al for these same clusters is in part due to the well-known light element anomalies in globular clusters (e.g., Kraft 1994; Mészáros et al. 2015). The lower [Mn/Fe] in metal-poor stars is consistent with previous work (e.g., Wallerstein 1962; Gratton 1989) using 1-dimensional models that assume local thermodynamic equilibrium.

- The increased scatter at lower metallicities is not entirely the result of actual inhomogeneities in cluster members, as there are increasing uncertainties associated with the weaker lines in more metal-poor stars. The error estimates reported in DR13 for these stars track the measured rms reasonably well, especially for errors in $[X/Fe] > 0.1$ dex, and therefore provide a useful guide for abundance ratios that are not well-determined (H16). On top of this, the ASPCAP methodology breaks down at some level for stars in which abundances within a given "abundance group" (e.g., the alpha-elements) depart from solar abundance ratios, as is the case for second-generation stars in metal-poor globular clusters (Mészáros et al. 2015).
- ASPCAP reports the parameters of the best-fitting model in χ^2 space. It does not currently report non-detections and upper limits. Therefore, most reported abundances for elements such as P that show $\sim$1 dex scatter in Figure 9 are based on fits to noise in the spectrum and do not reflect actual abundances. Abundances for such elements should not be used unless they are confirmed by visual inspection. They are reported because for a certain range in metallicity and temperature, the lines can be detected and interesting chemistry exposed (e.g., Hawkins et al. 2016).
- The disagreement between the [Ti/Fe] value based on Ti I lines and Ti II lines is yet to be resolved. We are currently investigating the choice of lines (as noted by Hawkins et al. 2016) and the effect of 3-D and NLTE corrections.
- The mean value and rms in Figure 9 were calculated using stars with $4100\text{K} < T_{\text{eff}} < 5000\text{K}$. The scatter becomes noticeably worse if the warmest or coolest stars in the clusters are included. Warmer stars have weaker lines in general in the H-band and the coolest stars are affected by the issues with the cool grid (see below).

The elements included in DR13 are by no means the only elements/species with lines present in the H-band amenable to abundance analysis. Hawkins et al. (2016), for example, independently derives Yb, along with many other elements, for the APOKASC sample (Pinsonneault et al. 2014). We expect to include additional elements in upcoming data releases.

7.3. *Synthetic Spectral Grids at $T_{\text{eff}} < 3500K$ and with Rotational Broadening*

In DR10-12, the synthetic spectral grid used by ASPCAP (Mészáros et al. 2012; Zamora et al. 2015) was restricted to temperatures hotter than 3500K because Kurucz model atmospheres are not available at cooler temperatures. However, many important APOGEE targets have cooler temperatures, including the luminous metal-rich M-giants in the bulge, cool asymptotic giant branch stars, and M dwarf planet hosts. Therefore, we used custom MARCS (Gustafsson et al. 2008) atmospheres provided by B. Edvardsson (private communication) to construct new synthetic spectra. For the stellar atmospheres for the giants, the atmospheres are spherical, otherwise they are plane-parallel. The Kurucz model grid and the new MARCS model grid overlap between 3500-4000K. In this region, there are some systematic differences between the results from the two grids; to provide homogeneous results, DR13 adopts the parameters and abundances from the analysis with the Kurucz grid.

Figure 10 shows the current parameter space in T_{eff}, log g and [M/H] covered by Data Release 13 stars. It is immediately apparent that the parameters derived from the MARCS grid do not match smoothly to the parameters from the Kurucz grid. Possible explanations include the switch from plane-parallel Kurucz to spherical MARCS for the giants and/or the large number of model atmospheres in the MARCS grid that failed to converge. Because ASPCAP requires a square grid of synthetic spectra, these "grid holes" were filled by adjacent model atmospheres. The linelist does not have FeH lines, which can be important features in the atmospheres of cool M dwarfs. We are investigating the size of the error caused by using incorrect model atmospheres in the grid, the possibilities of using alternative methods of interpolating and identifying the best-fit model, and the addition of FeH lines. H16 provides more details on the construction of the cool grid and the resulting stellar parameters. Nonetheless, Figure 10 illustrates the improved parameter space over DR12, which should aid in classifying M stars correctly as dwarfs or giants and separate the early M from the late M stars.

The APOGEE-1 sample is dominated by giants used to probe the chemical cartography of the Galaxy (Majewski et al. 2015). Fewer than 2% of red giants rotate at speeds detectable at the APOGEE spectrograph resolution (de Medeiros et al. 1996; Carlberg et al. 2011). Therefore the first versions of ASPCAP did not include rotational broadening as a dimension in the synthetic spectral grid, which substantially reduced the computing time. However, dwarf stars, of which there are >20,000 in APOGEE-1, are frequently rapidly rotating, especially if they are young. For DR13, we added a dimension to the synthetic spectral grid where spectra were broadened by a Gaussian kernel. To keep the computing time reasonable, and in acknowledgment of the small effect that C and N abundances have on the atmospheres of warm dwarfs, we fixed the [C/M] and [N/M] grids to solar values. The [C/Fe] and [N/Fe] values reported for dwarfs in DR13 are calculated from windows after the best-fit parameters are determined, in similar fashion to the other individual elements. Figure 11 shows the improvement in the stellar parameters for members of the Pleiades star cluster. Some of the dwarfs in this young cluster are rotating with $v \sin i > 50$ km/s. In DR12, ASPCAP found a best-fit solution for metal-poor stars. The shallower the lines because of rotational broadening, the more metal-poor the star was reported to be. With the

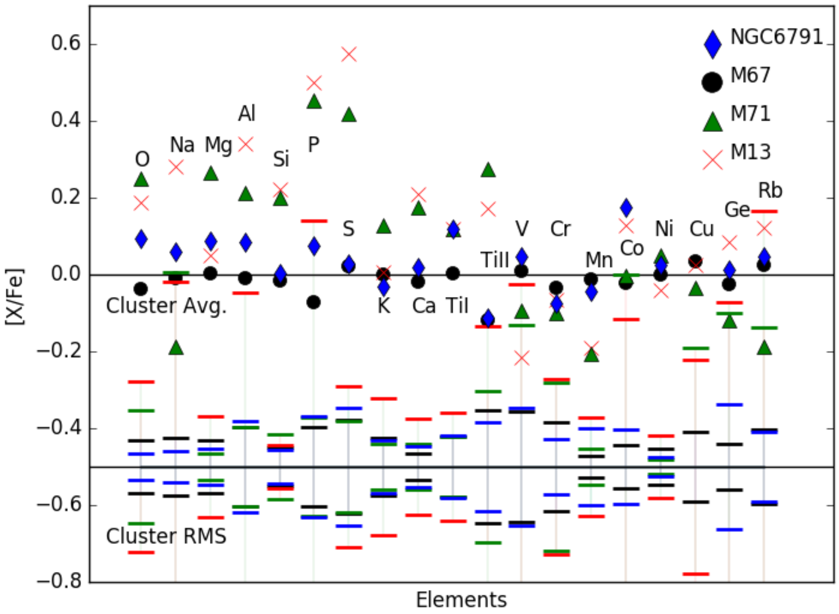

Fig. 9.— The abundances and RMS scatter in the stars with 4100K $< T_{\rm eff} <$ 5000K in 4 clusters spanning a range in metallicities (M13$= -1.58$, M71$= -0.82$, M67$= 0.06$, NGC 6791$= 0.37$ (Holtzman et al. 2015). The RMS is shown offset from the mean value points by -0.5 dex (indicated by solid line) and connected for the same element by vertical lines for clarity. C and N are not included because their values in a cluster change depending of the evolutionary state of the star as the result of first dredge-up (e.g., Masseron & Gilmore 2015).

DR13 grid, there is no longer a prominent trend in [M/H] with v sin i, and the mean value of the cluster is now at the expected metallicity.

7.4. *Data Access*

Data access via the CAS and SAS is similar to that for DR12 (Holtzman et al. 2015); "dr12" should be replaced with "dr13" in the pathname or DR13 as the context in CASJobs. Some of the tag/column names have been modified. While raw abundances are still given in the FELEM arrays, "calibrated" abundances are now presented in X_H and X_M arrays as well as in individual X_FE tags/columns. For dwarfs, there is now a column in the allStar fits file on the SAS or in the aspcapStar table on the CAS that reports the v sin i. DR13 also includes a new catalog of red clump stars based on the new ASPCAP parameters, following the method of Bovy et al. (2014), available at the location described in Table 2.

8. THE FUTURE

SDSS-IV will continue to add to the SDSS legacy of data and data analysis tools in upcoming data releases. For MaNGA, future data releases will include more data cubes of galaxies that are currently being observed. A data analysis pipeline is under active development and carries out continuum and emission line fitting to provide estimates of stellar and gas kinematics, emission line fluxes, and absorption line index measurements. We hope to make the resulting data products publicly available in future data releases. A data interface system including both web and python based tools is also under development. In addition, MaNGA has started a bright-time observing program, piggy-backing on APOGEE-2, to build a stellar library. These reduced optical stellar spectra will be included in a future data release. For eBOSS, future data releases will provide sufficient redshifts of LRG, ELG, and quasars to be of cosmological interest, on its way to the goals described in §1. TDSS and SPIDERS will also release many more spectra, redshifts, and classifications for variable and X-ray emitting objects, respectively. For APOGEE-2, the next data release (DR14) will contain spectra from the APOGEE-2N spectrograph at APO observed under SDSS-IV, and subsequent DRs will provide spectra taken both with the APOGEE-2N and the APOGEE-2S spectrograph at LCO. In addition to observing red giants as the main target category, data will be obtained for RR Lyrae stars in the bulge, dwarf spheroidal galaxies, the Magellanic Clouds, *Kepler* Objects of Interest, and targets in the K2 fields.

9. ACKNOWLEDGEMENTS

We would like to thank the Center for Data Science (`http://cds.nyu.edu`) at New York University for their hospitality during DocuFeest 2016.

Funding for the Sloan Digital Sky Survey IV has been provided by the Alfred P. Sloan Foundation, the U.S. Department of Energy Office of Science, and the Participating Institutions. SDSS-IV acknowledges support and resources from the Center for High-Performance Computing at the University of Utah. The SDSS web site is www.sdss.org.

SDSS-IV is managed by the Astrophysical Research

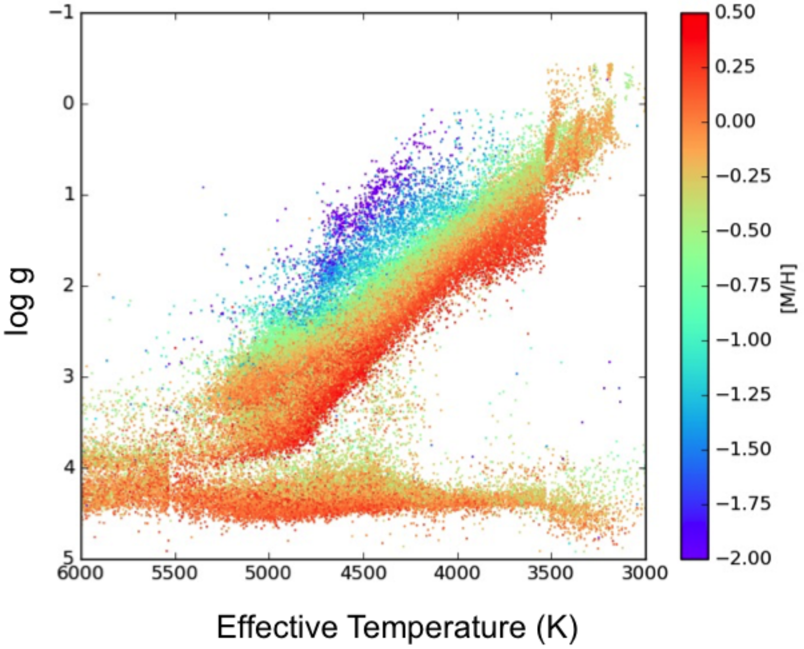

Fig. 10.— The Hertzsprung-Russell diagram for all DR13 APOGEE-1 stars. The calibrated gravities and temperatures are used. The cool stars now clearly fall into dwarf and giant categories, but the stellar parameters do not merge smoothly onto the warmer Kurucz-based grid.

Consortium for the Participating Institutions of the SDSS Collaboration including the Brazilian Participation Group, the Carnegie Institution for Science, Carnegie Mellon University, the Chilean Participation Group, the French Participation Group, Harvard-Smithsonian Center for Astrophysics, Instituto de Astrofísica de Canarias, The Johns Hopkins University, Kavli Institute for the Physics and Mathematics of the Universe (IPMU) / University of Tokyo, Lawrence Berkeley National Laboratory, Leibniz Institut für Astrophysik Potsdam (AIP), Max-Planck-Institut für Astronomie (MPIA Heidelberg), Max-Planck-Institut für Astrophysik (MPA Garching), Max-Planck-Institut für Extraterrestrische Physik (MPE), National Astronomical Observatory of China, New Mexico State University, New York University, University of Notre Dame, Observatário Nacional / MCTI, The Ohio State University, Pennsylvania State University, Shanghai Astronomical Observatory, United Kingdom Participation Group, Universidad Nacional Autónoma de México, University of Arizona, University of Colorado Boulder, University of Oxford, University of Portsmouth, University of Utah, University of Virginia, University of Washington, University of Wisconsin, Vanderbilt University, and Yale University.

REFERENCES

Abazajian, K. N., Adelman-McCarthy, J. K., Agüeros, M. A., et al. 2009, ApJS, 182, 543
Alam, S., Albareti, F. D., Allende Prieto, C., et al. 2015, ApJS, 219, 12
Alam, S., Ata, M., Bailey, S., et al. 2016, arXiv:1607.03155
Alvarez, R., & Plez, B. 1998, A&A, 330, 1109
Baumgartner, W. H., Tueller, J., Markwardt, C. B., et al. 2013, ApJS, 207, 19
Belfiore, F., Maiolino, R., Bundy, K., et al. 2015, MNRAS, 449, 867
Belfiore, F., Maiolino, R., Maraston, C., et al. 2016, MNRAS, 461, 3111
Blanton, M. R., Schlegel, D. J., Strauss, M. A., et al. 2005, AJ, 129, 2562
Blanton, M. R., Kazin, E., Muna, D., Weaver, B. A., & Price-Whelan, A. 2011, AJ, 142, 31
Bolton, A. S., Schlegel, D. J., Aubourg, É., et al. 2012, AJ, 144, 144
Bovy, J., Nidever, D. L., Rix, H.-W., et al. 2014, ApJ, 790, 127
Bovy, Jo, Hogg, D. W., & Roweis, S. T. 2011, Annals of Applied Statistics, 5,
Bovy, J., Hennawi, J. F., Hogg, D. W., et al. 2011, ApJ, 729, 141
Bowen, I. S., & Vaughan, A. H., Jr. 1973, Appl. Opt., 12, 1430
Bundy, K., Bershady, M. A., Law, D. R., et al. 2015, ApJ, 798, 7
Carlberg, J. K., Majewski, S. R., Patterson, R. J., et al. 2011, ApJ, 732, 39
Cheung, E., Bundy, K., Cappellari, M., et al. 2016, Nature, 533, 504
Cluver, M. E., Jarrett, T. H., Hopkins, A. M., et al. 2014, ApJ, 782, 90
Comparat, J., Delubac, T., Jouvel, S., et al. 2015, arXiv:1509.05045
Dalcanton, J. J., Williams, B. F., Seth, A. C., et al. 2009, ApJS, 183, 67
Dawson, K. S., Schlegel, D. J., Ahn, C. P., et al. 2013, AJ, 145, 10
Dawson, K. S., Kneib, J.-P., Percival, W. J., et al. 2016, AJ, 151, 44
de Medeiros, J. R., Da Rocha, C., & Mayor, M. 1996, A&A, 314, 499
Delubac, T., Bautista, J. E., Busca, N. G., et al. 2015, A&A, 574, A59
Doi, M., Tanaka, M., Fukugita, M., et al. 2010, AJ, 139, 1628
Drory, N., MacDonald, N., Bershady, M. A., et al. 2015, The Astronomical Journal, 149, 77

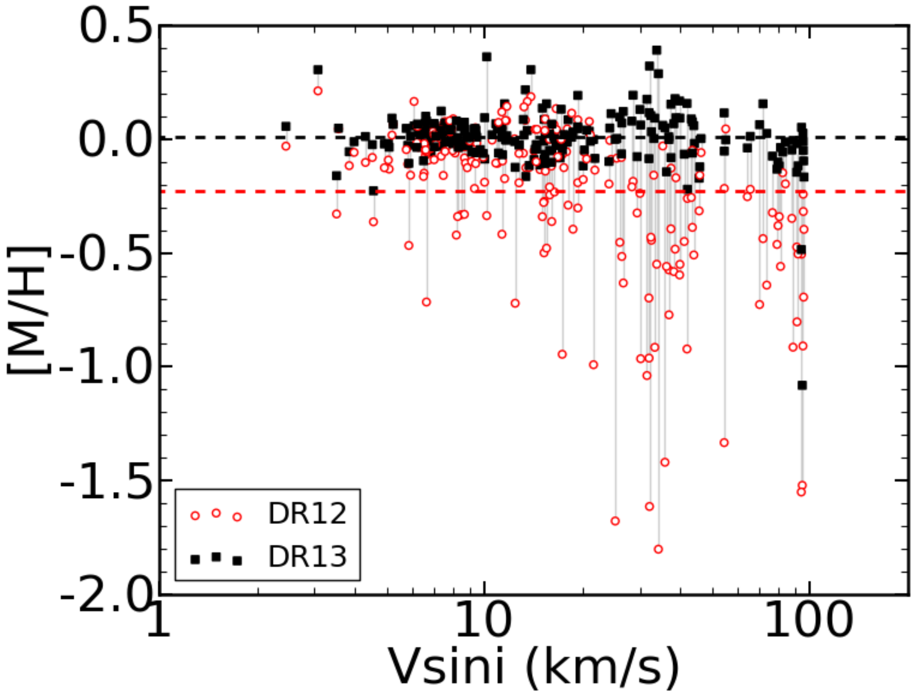

Fig. 11.— A comparison of the [M/H] derived for Pleiades cluster dwarfs from DR12 (red open circles) and DR13 (black filled squares). The Pleiades has many rapidly spinning stars with rotationally broadened, shallow lines. When analyzed with the DR12 version of ASPCAP, which did not include rotational broadening, the best χ^2 fit for the high v sin i stars was achieved for synthetic spectra with metallicity much lower than that known for the Pleiades. Therefore, the cluster average was sub-solar (red line). In DR13, where the dwarfs are run through a grid that includes a v sin i dimension, all Pleiades stars fall close to the correct value (black line), regardless of broadening.

Eisenstein, D. J., Zehavi, I., Hogg, D. W., et al. 2005, ApJ, 633, 560

Eisenstein, D. J., Weinberg, D. H., Agol, E., et al. 2011, AJ, 142, 72

Finkbeiner, D. P., Schlafly, E. F., Schlegel, D. J., et al. 2016, ApJ, 822, 66

Fitzpatrick, E. L. 1999, PASP, 111, 63

Frieman, J. A., Bassett, B., Becker, A., et al. 2008, AJ, 135, 338

Fukugita, M., Ichikawa, T., Gunn, J. E., et al. 1996, AJ, 111, 1748

García Pérez, A. E., Allende Prieto, C., Holtzman, J. A., et al. 2016, AJ, 151, 144

Geha, M., Blanton, M. R., Yan, R., & Tinker, J. L. 2012, ApJ, 757, 85

Gratton, R. G. 1989, A&A, 208, 171

Gunn, J. E., Carr, M., Rockosi, C., et al. 1998, AJ, 116, 3040

Gunn, J. E., Siegmund, W. A., Mannery, E. J., et al. 2006, AJ, 131, 2332

Guo, Q., White, S., Boylan-Kolchin, M., et al. 2011, MNRAS, 413, 101

Gustafsson, B., Edvardsson, B., Eriksson, K., et al. 2008, A&A, 486, 951

Hawkins, K., Masseron, T., Jofre, P., et al. 2016, arXiv:1604.08800

Hinkle, K., Wallace, L., & Livingston, W. 1995, PASP, 107, 1042

Holincheck, A. J., Wallin, J. F., Borne, K., et al. 2016, MNRAS, 459, 720

Jansen, F., Lumb, D., Altieri, B., et al. 2001, A&A, 365, L1

Jarrett, T. H., Masci, F., Tsai, C. W., et al. 2013, AJ, 145, 6

Holtzman, J. A., Shetrone, M., Johnson, J. A., et al. 2015, AJ, 150, 148

Kaiser, N., Burgett, W., Chambers, K., et al. 2010, Proc. SPIE, 7733, 77330E

Kaiser, N., Aussel, H., Burke, B. E., et al. 2002, Proc. SPIE, 4836, 154

Kraft, R. P. 1994, PASP, 106, 553

Lang, D., Hogg, D. W., & Schlegel, D. J. 2016, AJ, 151, 36

Law, D. R., Cherinka, B., Yan, R., et al. 2016, ArXiv e-prints, arXiv:1607.08613

Law, D. R., Yan, R., Bershady, M. A., et al. 2015, The Astronomical Journal, 150, 19

Law, N. M., Kulkarni, S. R., Dekany, R. G., et al. 2009, PASP, 121, 1395

Li, C., Wang, E., Lin, L., et al. 2015, ApJ, 804, 125

Li, C., Kauffmann, G., Jing, Y. P., et al. 2006, MNRAS, 368, 21

Li, N., & Thakar, A. R. 2008, Computing in Science and Engineering, 10, 18

Licquia, T. C., Newman, J. A., & Brinchmann, J. 2015, ApJ, 809, 96

Livingston, W., & Wallace, L. 1991, An atlas of the solar spectrum in the infrared from 1850 to 9000 cm-1 (1.1 to 5.4 micrometer)

Majewski, S. R., Schiavon, R. P., Frinchaboy, P. M., et al. 2015, ArXiv e-prints, arXiv:1509.05420

Masseron, T., & Gilmore, G. 2015, MNRAS, 453, 1855

Meléndez, J., & Barbuy, B. 1999, ApJS, 124, 527

Menzel, M.-L., Merloni, A., Georgakakis, A., et al. 2016, MNRAS, 457, 110

Mészáros, S., Martell, S. L., Shetrone, M., et al. 2015, AJ, 149, 153

Mészáros, S., Holtzman, J., García Pérez, A. E., et al. 2013, AJ, 146, 133

Mészáros, S., Allende Prieto, C., Edvardsson, B., et al. 2012, AJ, 144, 120

Morganson, E., Green, P. J., Anderson, S. F., et al. 2015, ApJ, 806, 244

Mullaney, J. R., Alexander, D. M., Fine, S., et al. 2013, MNRAS, 433, 622

Myers, A. D., Palanque-Delabrouille, N., Prakash, A., et al. 2015, ApJS, 221, 27

Nidever, D. L., Holtzman, J. A., Allende Prieto, C., et al. 2015, AJ, 150, 173

Paegert, M., Stassun, K. G., De Lee, N., et al. 2015, AJ, 149, 186

Palanque-Delabrouille, N., Magneville, C., Yèche, C., et al. 2016, A&A, 587, A41

Palanque-Delabrouille, N., Yeche, C., Myers, A. D., et al. 2011, A&A, 530, A122

Piffaretti, R., Arnaud, M., Pratt, G. W., Pointecouteau, E., & Melin, J.-B. 2011, A&A, 534, A109

Pinsonneault, M. H., Elsworth, Y., Epstein, C., et al. 2014, ApJS, 215, 19

Plez, B. 2012, Astrophysics Source Code Library, ascl:1205.004

Prakash, A., Licquia, T. C., Newman, J. A., et al. 2016, ApJS, 224, 34

Predehl, P., Andritschke, R., Becker, W., et al. 2014, in Proc. SPIE, Vol. 9144, Space Telescopes and Instrumentation 2014: Ultraviolet to Gamma Ray, 91441T

Raichoor, A., Comparat, J., Delubac, T., et al. 2016, A&A, 585, A50

Ruan, J. J., Anderson, S. F., Green, P. J., et al. 2016, ArXiv e-prints, arXiv:1602.02752

Runnoe, J. C., Cales, S., Ruan, J. J., et al. 2016, MNRAS, 455, 1691

Ryde, N., & Schultheis, M. 2015, A&A, 573, A14

Saxton, R. D., Read, A. M., Esquej, P., et al. 2008, A&A, 480, 611

Schlafly, E. F., Finkbeiner, D. P., Jurić, M., et al. 2012, ApJ, 756, 158

Schlafly, E. F., & Finkbeiner, D. P. 2011, ApJ, 737, 103

Schlegel, D. J., Finkbeiner, D. P., & Davis, M. 1998, ApJ, 500, 525

Sesar, B., Ivezić, Ž., Lupton, R. H., et al. 2007, AJ, 134, 2236

Shetrone, M., Bizyaev, D., Lawler, J. E., et al. 2015, ApJS, 221, 24

Shao, L., Kauffmann, G., Li, C., Wang, J., & Heckman, T. M. 2013, MNRAS, 436, 3451

Smee, S. A., Gunn, J. E., Uomoto, A., et al. 2013, AJ, 146, 32

Thakar, A. R. 2008, Computing in Science and Engineering, 10, 9

Thakar, A. R., Szalay, A., Fekete, G., & Gray, J. 2008, Computing in Science and Engineering, 10, 30

Thomas, N., Ge, J., Grieves, N., Li, R., & Sithajan, S. 2016, PASP, 128, 045003

Ting, Y.-S., Conroy, C., & Rix, H.-W. 2016, ApJ, 816, 10

Vasudevan, R. V., & Fabian, A. C. 2009, MNRAS, 392, 1124

Voges, W., Aschenbach, B., Boller, T., et al. 1999, A&A, 349, 389

Wallerstein, G. 1962, ApJS, 6, 407

Wilkinson, D. M., Maraston, C., Thomas, D., et al. 2015, MNRAS, 449, 328

Wright, E. L., Eisenhardt, P. R. M., Mainzer, A. K., et al. 2010, AJ, 140, 1868-1881

Yan. R., Bundy, K., Law, D. R., et al. 2016, ArXiv e-prints, arXiv:1607.08613

Yan, R., Tremonti, C., Bershady, M. A., et al. 2016, AJ, 151, 8

Yan, R., Tremonti, C., Bershady, M. A., et al. 2015, The Astronomical Journal, 151, 8

Yang, X., Mo, H. J., van den Bosch, F. C., et al. 2007, ApJ, 671, 153

Yanny, B., Rockosi, C., Newberg, H. J., et al. 2009, AJ, 137, 4377

York, D. G., Adelman, J., Anderson, Jr., J. E., et al. 2000, AJ, 120, 1579

Zamora, O., García-Hernández, D. A., Allende Prieto, C., et al. 2015, AJ, 149, 181

Zasowski, G., Johnson, J. A., Frinchaboy, P. M., et al. 2013, AJ, 146, 81

Zhai, Z., Tinker, J. L., Hahn, C., et al. 2016, arXiv:1607.05383

Zhu, G. B., Comparat, J., Kneib, J.-P., et al. 2015, ApJ, 815, 48

Zou, H., Zhou, X., Jiang, Z., et al. 2016, AJ, 151, 37